Structure of heavy-metal sorbed birnessite: Part 1. Results from X-ray diffraction

Bruno Lanson,[1,*] Victor A. Drits,[1,2] Anne-Claire Gaillot,[1] Ewen Silvester,[1,3] Alain Plançon,[4] and Alain Manceau[1]

[1]Environmental Geochemistry Group, LGIT, Maison des Géosciences, BP53, University of Grenoble-CNRS, 38041 Grenoble Cedex 9, France
[2]Geological Institute, Russian Academy of Sciences, 7 Pyzhevsky street, 109017 Moscow, Russia
[3]CSIRO, Division of Minerals, Box 312, Clayton South, 3169, Australia
[4]ISTO, University of Orléans-CNRS, 1A rue de la Férolleire, 45071 Orléans Cedex 2, France

Abstract

The structure of heavy-metal sorbed synthetic birnessites (MeBi) was studied by powder X-ray diffraction (XRD) using a trial-and-error fitting procedure to improve our understanding of the interactions between buserite/birnessite and environmentally important heavy metals (Me) including Pb, Cd, and Zn. MeBi samples were prepared at different surface coverages by equilibrating at pH 4 a Na-rich buserite (NaBu) suspension in the presence of the desired aqueous metal.

Two main types of experimental XRD patterns were obtained as a function of the Me cations sorbed from solution, which exert a strong control on layer stacking sequence, as well as on the location and coordination of Me: (1) CdBi and PbBi samples correspond to a one-layer hexagonal (1H) structure, $AbC_{b'A'}{}^{C'b'}AbC...$, and (2) ZnBi exhibits a one-layer monoclinic (1M) structure in which adjacent layers are shifted by $+\mathbf{a}/3$, $AbC_{b'A'c'}BcA_{c'B'a'}CaB_{a'C'b'}AbC$.

Simulated XRD patterns show that octahedral layers contain 0.833 Mn cations (Mn^{4+} and Mn^{3+}) and 0.167 vacant octahedra; $Mn^{3+}_{interlayer}$ and adsorbed $Me_{interlayer}$ compensate for the layer charge deficit. $Mn^{3+}_{interlayer}$ is octahedrally coordinated in all samples and is located above or below vacant layer octahedra sharing three O_{layer} with neighboring Mn_{layer} octahedra to form a triple-corner surface complex (^{VI}TC sites). In ZnBi and CdBi samples, $Me_{interlayer}$ is also located in TC sites; all Cd is octahedrally coordinated whereas about 30% of Zn is tetrahedrally coordinated (^{IV}TC sites). In PbBi samples, all Pb is octahedrally coordinated, most of these cations (~75%) being located in TC sites. Additional Pb is located above or below empty tridentate cavities, sharing three edges with neighboring Mn_{layer} octahedra (^{VI}TE sites).

Structural formulae calculated for each sample show that during the NaBu-to-MeBi structural transformation, interlayer Na^+ and Mn^{2+} are replaced by Me and H^+ adsorbed from solution, whereas $Mn^{3+}_{interlayer}$ resulting from the equilibration of NaBu at low pH is less affected. Sorption of divalent Me above and below vacant layer sites provides optimal conditions for local charge compensation in MeBi.

Introduction

Buserite and birnessite are the most common layered hydrous Mn oxides, or phyllomanganates, in natural environments. Birnessite is the main Mn-bearing phase in soils (Taylor et al. 1964; Chukhrov and Gorshkov 1981), and in marine nodules, coatings, and crusts (Burns and Burns 1976; Glover 1977; Chukhrov et al. 1978, 1985, 1989; Drits et al. 1985). Birnessite is also an essential component of some Mn-rich ore deposits (Chukhrov et al. 1987, 1989; Post 1999).

The structures of these minerals consist of layers of edge-sharing Mn-(O,OH) octahedra. Buserite has a 10 Å periodicity along the **c*** axis with exchangeable cations and two layers of H_2O molecules in its interlayer region to compensate for the negative layer charge that arises mostly from the coexistence of heterovalent Mn cations in the octahedral layers (Silvester et al. 1997). Partial dehydration of buserite leads to the formation of 7 Å birnessite with a single layer of H_2O molecules and

various interlayer cations (Burns and Burns 1977, 1978; Chukhrov et al. 1978, 1989; Cornell and Giovanoli 1988). Buserite and birnessite have remarkable cation exchange (Healy et al. 1966; Murray 1974; Balistrieri and Murray 1982; Stumm 1992; Le Goff et al. 1996), sorption (Gray and Malati 1979; Catts and Langmuir 1986; Paterson et al. 1994; Tu et al. 1994; Appelo and Postma 1999), and redox properties (Oscarson et al. 1983; Stone and Morgan 1984; Stone and Ulrich 1989; Manceau and Charlet 1992; Bidoglio et al. 1993; Silvester et al. 1995; Manceau et al. 1997; Pizzigallo et al. 1998; Daus et al. 2000; Nico and Zasoski 2000; Chorover and Amistadi 2001).

The ability of buserite and birnessite to fix trace elements (Co, Pb, Cd, Cu, Zn, …) ranks these minerals among the most efficient sorbents of heavy metals (McKenzie 1967, 1980; Burns and Burns 1976; Bendell-Young and Harvey 1992; Post 1999; Manceau et al. 2000). As a consequence, despite its low natural abundance, birnessite exerts an essential role in the partitioning of heavy metals (Me) in soils and in both marine and continental sediments (Taylor and McKenzie 1966; McKenzie 1967, 1980; Manceau et al. 2000 and references therein). Be-

---

* E-mail: Bruno.Lanson@obs.ujf-grenoble.fr

cause serious environmental problems may result from an excessive concentration of heavy metals in soils and aquatic systems, it is essential to have a better understanding, at the atomic level, of the interactions between different heavy metals and phyllomanganates. However, in nature, birnessite is typically disordered and occurs in a finely dispersed state, commonly mixed with other phases such as phyllosilicates and Fe oxyhydroxides. As a result, crystal-chemical studies of heavy-metal bearing birnessites and buserites are very limited, and both the location of heavy metals in the phyllomanganate structure and the mechanism of their sorption remain poorly understood.

Monomineralic buserite and birnessite with a high degree of structural order are easily synthesized under various laboratory conditions (Giovanoli et al. 1970a, 1970b; Strobel et al. 1987; Cornell and Giovanoli 1988; Ching et al. 1995; Chen et al. 1996; Luo and Suib 1997; Kim et al. 1999). Because these synthetic varieties are considered analogs of natural buserites/birnessites (Manceau et al. 2000), their use is preferred in determining the structural characteristics of heavy-metal bearing birnessites as well as the reaction mechanisms for absorption of heavy metals. The present study aims at a better understanding of the interaction between synthetic buserite/birnessite structures and environmentally important Me such as Pb, Cd, and Zn. Special attention is paid to the structural modifications induced by the presence of sorbed Me cations in the birnessite structure.

Recent crystal-chemical studies of synthetic buserite and birnessite by complementary diffraction and spectroscopic methods have provided important new insights on the structure of these compounds (Chukhrov et al. 1985; Post and Veblen 1990; Manceau and Charlet 1992; Kuma et al. 1994; Drits et al. 1997, 1998a; Manceau et al. 1997; Silvester et al. 1997; Lanson et al. 2000). This new information will serve as a basis for the present detailed crystal-chemical studies of Me-sorbed birnessite (MeBi). Application of complementary techniques such as quantitative powder X-ray diffraction (XRD), selected-area electron diffraction (SAED), energy-dispersive analysis (EDA), chemical analysis, and powder as well as polarized extended X-ray absorption fine-structure spectroscopy (EXAFS) was also critical in solving the different aspects of structural chemistry of heavy metals in birnessite structures.

EXPERIMENTAL METHODS

NaBu used for this study was synthesized following the protocol of Giovanoli et al. (1970a). The solid phase was washed by centrifugation until the supernatant pH was 9–10. The sorption of various Me cations was achieved by adding an $Me(NO_3)_n$ solution (Zn, Pb, Cd, and Cu) while equilibrating a NaBu suspension at pH 4. All samples were prepared in an Ar-gas-saturated and constant ionic strength ($0.1 \ mol/dm^3 \ NaNO_3$) aqueous medium at 25 °C as described by Silvester et al. (1997). As NaBu was not pre-equilibrated at pH 4, NaBu-to-HBi transformation at low pH and Me sorption occurred simultaneously (Manceau et al. 1997). Variation of the initial Me concentrations in solution allowed the generation of different Me/Mn ratios in the solids. After several hours of equilibration, all samples were filtered and dried, yielding MeBi solids. Total

Me, Na, and Mn concentrations were determined by inductively coupled plasma spectroscopy (ICP, Perkin Elmer Optima 3300DV) after dissolution of the dried solids in NH_3OHCl. Me/Mn ratios determined from these analyses are used hereafter to characterize the different MeBi samples.

Powder XRD patterns were recorded using a Bruker D5000 powder diffractometer equipped with a Kevex Si(Li) solid-state detector and CuKα radiation. Intensities were measured at a 0.04 °2θ interval using a 30–50 s counting time per step.

Simulation of XRD patterns

The structural disorder induced by random and well-defined stacking faults decreases the efficiency of conventional X-ray methods of structural analysis, including the Rietveld method. Alternatively, the actual structure of defective layered compounds can be modeled using the mathematical formalism described in detail by Drits and Tchoubar (1990) to simulate experimental XRD patterns. This trial-and-error simulation procedure was successfully used to propose crystal structure models for several natural and synthetic birnessites (Chukhrov et al. 1985; Manceau et al. 1997; Drits et al. 1998a; Lanson et al. 2000). Details on the program used to simulate XRD patterns and on the fitting procedure are given by Drits et al. (1998a). Specifically, the lognormal coherent scattering domain size distribution along the **c** axis was quantified by two parameters: the average and maximum number of layers (Drits et al. 1998b). The agreement factors between experimental and calculated patterns were determined over the 35–65 °2θ CuKα range (2.55–1.45 Å) using the usual R_{WP} parameter. Calculations of XRD patterns were limited to 20l and 11l reflections (indexing based on an orthogonal base-centered unit cell) because these lines are the most sensitive to structural parameters of layered minerals, such as order/disorder in their stacking sequences (Brindley 1980). For each sample, the background was assumed to decrease linearly over the angular range considered, and preferred orientation of particles was considered as a variable parameter modeled using the function described by Drits and Tchoubar (1990).

RESULTS

Cation composition from ICP data

Table 1 lists the Me/Mn and Na/Mn atomic ratios determined for all Me-sorbed birnessite samples. The two Pb-containing birnessite samples (PbBi 6 and 58) differ in their 0.006 and 0.058 Pb/Mn ratios, and both samples contain a significant amount of Na, indicating that the Pb^{2+} and H^+ for Na^+ exchange was incomplete. Two of the four Zn-bearing birnessite specimens (ZnBi 122 and 128) have similar Zn/Mn ratios (0.122 and 0.128, respectively). A third ZnBi sample (ZnBi 69), which was prepared using a slower rate of pH decrease, has a Zn/Mn ratio half that of these two ZnBi samples, and a fourth sample has a very low Zn/Mn ratio (0.008, Table 1). In contrast to the PbBi samples, the low Na/Mn values determined for these four ZnBi samples indicate that almost all Na was replaced by Zn and protons. The Cd-sorbed birnessite sample (CdBi 106) has a 0.106 Cd/Mn ratio and a low amount of Na (Na/Mn = 0.006).

TABLE 1. $Mn_{interlayer}$, Me, and Na contents calculated for the two initial structure models from the Me/Mn and Na/Mn ratios determined by chemical analysis

Sample	Me/Mn	Na/Mn	N_Mn$_{interlayer}$		N_Me		N_Na$_{interlayer}$
			Model 1	Model 2	Model 1	Model 2	
ZnBi 8	0.008	0.017	0.159	0.159	0.008	0.016	0.017
ZnBi 69	0.069	0.011	0.102	0.133	0.065	0.067	0.010
ZnBi 122	0.122	0.007	0.058	0.110	0.109	0.115	0.006
ZnBi 128	0.128	0.021	0.053	0.106	0.113	0.121	0.019
PbBi 6	0.006	0.093	0.161	0.164	0.006	0.006	0.093
PbBi 58	0.058	0.067	0.112	0.139	0.055	0.056	0.064
CdBi 106	0.106	0.006	0.071	0.116	0.096	0.100	0.006
CuBi 156	0.156	0.043	0.032	0.050	0.135	0.234	0.038

Note: Relative error in the determination of the atomic ratios does not exceed 5%. N_Mn$_{interlayer}$, N_Me, and N_Na$_{interlayer}$ are derived from the measured concentrations using Equations 1 and 2 for both model 1 and model 2 (n = 1, 2, respectively).

Features of the experimental XRD patterns

Experimental XRD patterns of MeBi (Fig. 1) can be separated into three groups as a function of positions and profiles of their diffraction maxima. In the first group (Fig. 1a), XRD patterns exhibit reflections that can be indexed with a one-layer hexagonal (1H) unit cell (CdBi 106, PbBi 6 and 58 – Tables 2, 3). ZnBi samples 69, 122, and 128 make up the second group of samples (Fig. 1b), and their XRD patterns can be indexed with a one-layer monoclinic (1M) unit cell with $|c.cos\beta| = a/3$ (Tables 2 and 3). Sample ZnBi 8 defines the third group, as its XRD pattern contains very weak and extremely broad maxima, the positions of which cannot be indexed using 1H or 1M unit cells. The high degree of stacking disorder that is responsible for this XRD pattern (see below) prevented us from refining a structure model for this sample. Experimental XRD patterns of the three groups also differ in their reflection profiles, which are increasingly broadened from PbBi 58 to CdBi 106 and then to ZnBi, the broadest and most asymmetrical profiles being observed for ZnBi 8 (Fig. 1).

Unit-cell parameters for samples of the first two groups are given in Table 2, and experimental and calculated $d(hkl)$ values are compared in Table 3. Indexing was performed using a base-centered unit cell with $a = b\sqrt{3}$, as the layers have hexagonal symmetry in both 1H and 1M varieties. However, within each group, experimental XRD patterns exhibit some specific features. For example, experimental and calculated d(hkl) values almost coincide for PbBi 6 and 58, whereas the difference between $d_{cal}(20l, 11l)$ and $d_{exp}(20l, 11l)$ exceeds the experimental error (±0.001 Å) for CdBi 106, and ZnBi 122 and 128 (Table 3). The origin of this discrepancy is considered below.

Initial structure and composition of MeBi layers. To build up initial structure models for the various MeBi samples, the NaBu-to-MeBi transformation was assumed to follow the same reaction pathway as the NaBu-to-HBi transformation (Drits et al. 1997; Silvester et al. 1997; Lanson et al. 2000). In addition, the NaBu-to-MeBi transformation involves partial replacement of $Mn_{interlayer}$ by Pb^{2+}, Cd^{2+}, or Zn^{2+} cations sorbed from solution. All of these cations are larger than Mn^{4+}, and it is realistic to assume that they do not migrate into the vacant layer sites as they are not oxidized during the process (Manceau et al. 2002). Consequently, it was initially assumed that MeBi layers contain 0.833 Mn cations and 0.167 vacant layer sites regardless of the metal cation, as HBi layers. The similar values of a and b parameters determined for all MeBi samples including HBi (Table 2) support this hypothesis of a constant layer cation com-
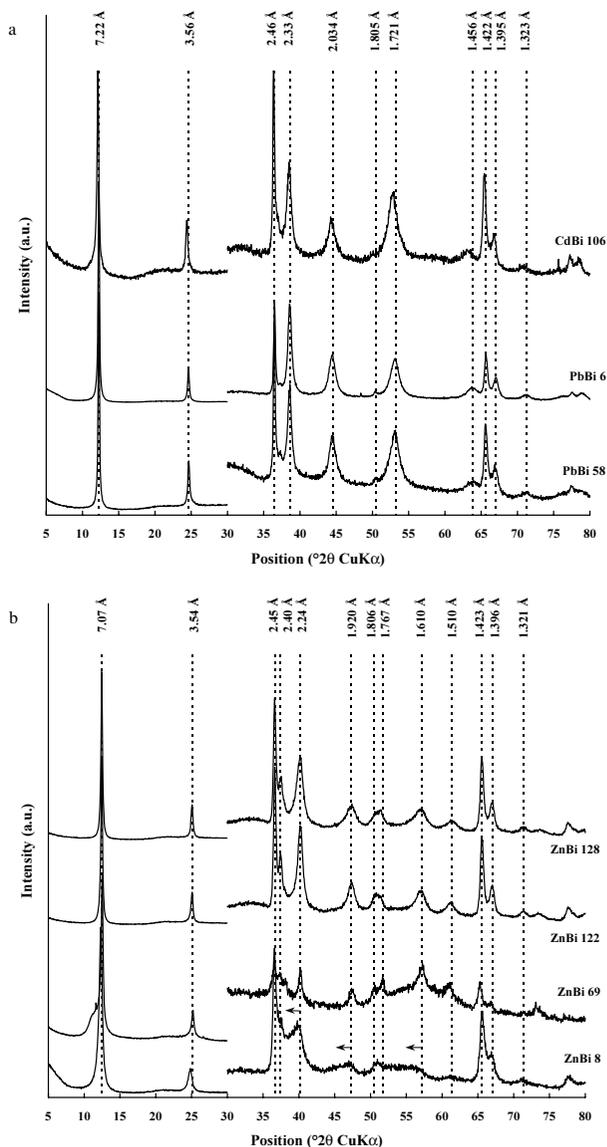

FIGURE 1. Experimental XRD patterns of the various MeBi samples. (**a**) Samples from the first group. (**b**) Samples from the second and third (ZnBi 8) groups. Arrows above reflections in the XRD pattern of ZnBi 8 show direction in which this reflection is shifted with respect to the position of the nearest *hkl* maximum of 1H MeBi samples. Intensity is enlarged by 2× (CdBi 106), 5×(PbBi 6 and 58, ZnBi 8, 122 and 128), or 10× (ZnBi 69) scale factors over the 30–80 °2θ range.

position. By analogy with HBi, $Mn_{interlayer}$ and Me were initially assumed to be octahedrally coordinated in MeBi, and $Mn_{interlayer}$ was assumed to be located either above or below vacant layer sites, sharing three O_{layer} with neighboring Mn_{layer} octahedra to form a triple-corner surface complex (^{VI}TC sites; Spadini et al. 1994). Two hypotheses were considered regarding the location of divalent Me with respect to these vacant layer sites. In the first model, Me was located either above or below vacant layer sites, whereas it was located above and below vacant layer sites in the second model. XRD patterns were calculated for these two starting models and compared with experimental ones.

The respective amounts of sorbed Me (N_Me) and $Mn_{interlayer}$ (N_$Mn_{interlayer}$) for these two models can be obtained from the Me/Mn ratios (ρ) determined from the chemical analysis (Table 1) as $ρ = N\_Me/(0.833 + N\_Mn_{interlayer})$. As a consequence:

$$N\_Me = nρ/(1 + nρ) \text{ and } N\_Mn_{interlayer} = 0.167 - N\_Me/n, \quad (1), (2)$$

with n = 1, 2 for the first and second models, respectively. Calculated N_Me values for the two models are listed in Table 1. Initially, coordinates of O_{layer}, $Mn_{interlayer}$, and bound H_2O molecules were assumed to be similar to those in HBi pH 2–5

TABLE 2. Unit-cell parameters obtained from the indexing of d/(hkl) values for the various samples

Sample	a	B	csinβ	β
HBi pH4*	4.933(3)†	2.848(2)	7.186(5)	90°
ZnBi 122	4.930(3)	2.846(2)	7.070(5)	76.9°
ZnBi 128	4.929(3)	2.846(2)	7.070(5)	76.9°
PbBi 6	4.926(3)	2.844(2)	7.228(5)	90°
PbBi 58	4.926(3)	2.844(2)	7.218(5)	90°
CdBi 106	4.933(3)	2.848(2)	7.288(5)	90°

* From Lanson et al. (2000).
† E.s.d. on unit-cell parameters based on estimated accuracy on peak poitions (±0.001 Å).

(Lanson et al. 2000).

Thus, to define fully the initial model for the various MeBi specimens, z-coordinates of Me and associated H_2O molecules (H_2O_{Me}) are the only parameters to be determined, as their other coordinates are deduced from the layer hexagonal symmetry and from anion close packing. The initial z-coordinates of Me and H_2O_{Me} can be estimated using typical Me-O and Me-H_2O bond lengths for ^{VI}Me. These inter-atomic distances calculated from effective ionic radii (Shannon 1976) are equal to 2.50, 2.30, and 2.10 Å, for Pb^{2+}, Cd^{2+}, and Zn^{2+}, respectively. Assuming that the structure is close packed, the following equations may be deduced from the hexagonal symmetry of the layer:

$$z\_Me = z\_O_{layer} + \sqrt{d^2(Me-O) - \frac{b^2}{3}} = z\_O_{layer} + Δz, \text{ and} \quad (3)$$

$$z\_H_2O_{Me} = z\_O_{layer} + 2·Δz \quad (4)$$

Finally, interlayer Na cations and H_2O molecules not coordinated to interlayer cations were located as in HBi (Lanson et al. 2000).

Layer stacking. Layer stacking in MeBi samples is described in terms of base-centered unit cells having their origin in the center of symmetry of the layer, that is, in the center of a layer octahedron (Mn_{layer} site). Using the anion close-packing notation, the sequence of birnessite layers in the 1H structure may be written $AbC_{b'A'}{}^{C'b'}AbC…$, where A and C represent sites for O_{layer}, A' and C' are H_2O interlayer sites, and b and b' are Mn_{layer} and $Mn_{interlayer}$ plus Me sites, respectively. Sub- and superscripts refer to interlayer species linked to the lower and upper layers, respectively. The positive direction of the **a** axis is defined by the AbC sequence. The positions of reflections observed for the 1M phase may result from two alternative layer

TABLE 3. Indexing of the experimental XRD patterns of MeBi

Sample	PbBi 6		PbBi 58		CdBi 106		ZnBi 122		ZnBi 128	
	Exp.	Calc.	Exp.	Calc.	Exp.	Calc.	Exp.	Calc.	Exp.	Calc.
001	7.210	7.228	7.201	7.218	7.285	7.288	7.097	7.070	7.092	7.070
002	3.612	3.624	3.608	3.609	3.644	3.644	3.548	3.535	3.552	3.535
110/200	2.461	2.463	2.463	2.463	2.469	2.466				
110/201							2.451	2.450	2.453	2.448
111/200							2.401	2.402	2.399	2.401
111/201	2.331	2.331	2.331	2.331	2.335	2.336				
11-1/202							2.242	2.237	2.243	2.235
112/202	2.037	2.035	2.036	2.034	2.041	2.043				
11-2/203							1.919	1.913	1.919	1.912
113/20-2							1.796	1.806	1.798	1.805
004	1.809	1.807					1.777	1.768	1.777	1.768
113/203	1.723	1.722	1.724	1.721	1.730	1.731				
11-3/204							1.615	1.608	1.616	1.608
114/20-3							1.515	1.519	1.512	1.519
114/204	1.459	1.457	1.454	1.456	1.472	1.466				
311/020							1.423	1.424	1.423	1.423
310/020	1.421	1.422	1.422	1.422	1.425	1.424				
312/021							1.396	1.396	1.396	1.395
311/021	1.395	1.395	1.398	1.395	1.400	1.398				
31-1/022							1.321	1.321	1.321	1.320
312/022	1.323	1.323	1.321	1.323	1.327	1.326				
115/20-4							1.288	1.291	1.285	1.291
115/205	1.246	1.247								
221							1.229	1.231	1.229	1.230
220	1.230	1.231	1.231	1.231	1.234	1.233				
221	1.214	1.214			1.217	1.216				

Notes: $d_{calc}(hkl)$ values are calculated using the unit-cell parameters listed in Table 2; $d_{exp}(hkl)$ are measured experimentally.

sequences in which successive octahedral layers are shifted by either $+\mathbf{a}/3$ or $-\mathbf{a}/3$, as the indexing of ZnBi samples leads to $|c\cdot\cos\beta| = a/3$. Symbolically, these two possible 1M stacking sequences may be described by:

$$\text{AbC}_{b'A'c'}\text{BcA}_{c'B'a'}\text{CaB}_{a'C'b'}\text{AbC}\ldots \quad (c\cdot\cos\beta = +0.333\ a),\text{ and} \tag{5}$$

$$\text{AbC}_{b'A'}{}^{B'a'}\text{CaB}_{a'C'}{}^{A'c'}\text{BcA}_{c'B'}{}^{C'b'}\text{AbC}\ldots \quad (c\cdot\cos\beta = -0.333\ a) \tag{6}$$
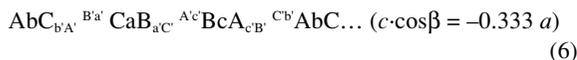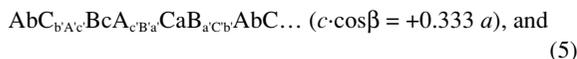
The first stacking sequence is similar to that of chalcophanite (Post and Appleman 1988) and of the accessory phase present in HBi pH 5 (Lanson et al. 2000), whereas the second layer sequence is similar to that of high pH NaBi (Post and Veblen 1990; Manceau and Charlet 1992; Lanson et al. 2002).

For each sample, XRD patterns were calculated for initial models 1 and 2 taking into account that PbBi and CdBi samples have an orthogonal layer stacking sequence, as does HBi, and that ZnBi has a 1M layer stacking with $+\mathbf{a}/3$ or $-\mathbf{a}/3$ interlayer displacement. Comparison of experimental and calculated XRD patterns showed that initial model 2 provides a better agreement for ZnBi and CdBi whereas model 1 better fits PbBi samples (data not shown). Therefore, henceforward structure models of PbBi correspond to model 1 in which Pb is located either above or below vacant layer octahedra, whereas in structure models of ZnBi and CdBi, Me is located above and below these sites. Figure 2 compares XRD patterns calculated for the initial layer model of ZnBi 122 with the two possible layer stacking sequences ($\pm\mathbf{a}/3$). The intensity distributions calculated for $20l$, $11l$ reflections differ dramatically for these two layer sequences, and experimental XRD patterns of ZnBi 122 and ZnBi 128 unambiguously correspond to the $+\mathbf{a}/3$ stacking sequence (Eq. 5).

Stacking faults. The presence of well-defined and/or random stacking faults is common in natural and synthetic layered minerals, including birnessites (see Drits and Tchoubar 1990, for a definition of well-defined and random stacking faults). Figure 3a compares the experimental XRD pattern of ZnBi 122 with the one calculated for the initial 1M structural model free of well-defined stacking faults, which is referred to hereafter as the defect-free model even though it contains random stacking faults. For this defect-free model, the calculated $20\overline{l},11(l+1)$, and $20l,11(\overline{l}-1)$ reflections (l being positive) are significantly shifted in comparison with the experimental peak positions to lower and higher 2θ values, respectively (Fig. 3a – Table 3). The diffraction effects described by Drits and McCarty (1996) for the random interstratification of layer fragments having the same thickness (but different interlayer displacement) provides an explanation for such a shift. Indeed, in such a case, the positions of the observed hkl reflections are located between neighboring hkl reflections of phases whose elementary components are interstratified. Similar diffraction effects have been observed and quantitatively interpreted for Ca-exchanged birnessite (Drits et al. 1998a) and for HBi prepared at different values of pH (Lanson et al. 2000).

Experimental $20l,11l_{\text{exp}}$ reflections are located between calculated $20\overline{l}, 11(l+1)_{\text{M}}$ and $20l,11l_{\text{H}}$ reflections (Fig. 3a). If one
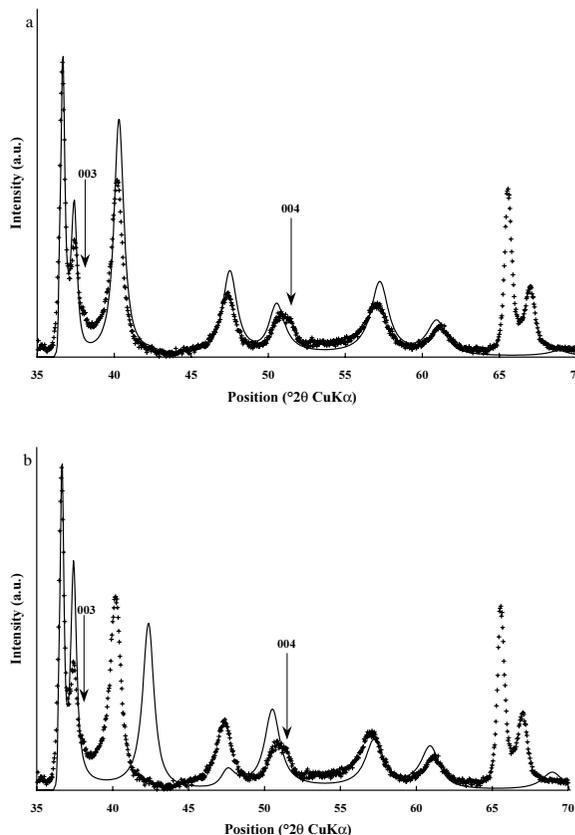

FIGURE 2. Comparison between experimental and calculated XRD patterns for ZnBi 122. Experimental data are shown as crosses. The XRD patterns calculated for the initial 1M layer model of ZnBi 122 and the two possible directions for the $a/3$ shift are shown on Figure 2a ($+\mathbf{a}/3$ shift) and Figure 2b ($-\mathbf{a}/3$ shift). Only $20l$, $11l$ reflections were calculated.

assumes that the 1M ZnBi 122 structure contains orthogonal layer pairs, positions of $20\overline{l},11(l+1)_{\text{M}}$, and $20l,11(\overline{l}-1)_{\text{M}}$ reflections should be shifted toward $20l,11l_{\text{H}}$ maxima in comparison with the defect-free ZnBi 122 (Fig. 3a). Accordingly, the best agreement between experimental and calculated $20l,11l$ reflection positions and profiles was obtained for a defective 1M ZnBi phase containing 12 and 15% of randomly interstratified orthogonal layer pairs in ZnBi 122 (Fig. 3b) and ZnBi 128, respectively.

In contrast to ZnBi samples, the initial agreement between experimental peak positions and those calculated for a defect-free 1H model was, at the first sight, satisfactory for the first group of samples (CdBi 106, PbBi 6 and 58). However, Figure 4a ($R_{\text{WP}} = 10.4\%$) shows that positions of $201,111_{\text{H}}$ and $202,112_{\text{H}}$ calculated for defect-free 1H CdBi are very slightly shifted toward lower 2θ values in comparison with the corresponding experimental reflections, most likely because of interstratification effects similar to those described for ZnBi 122. A small amount of monoclinic layer pairs, in which layers are shifted with respect to each other by $+\mathbf{a}/3$, induces a displacement of $201,111_{\text{H}}$ and $202,112_{\text{H}}$ reflections toward $202,11\overline{1}_{\text{M}}$
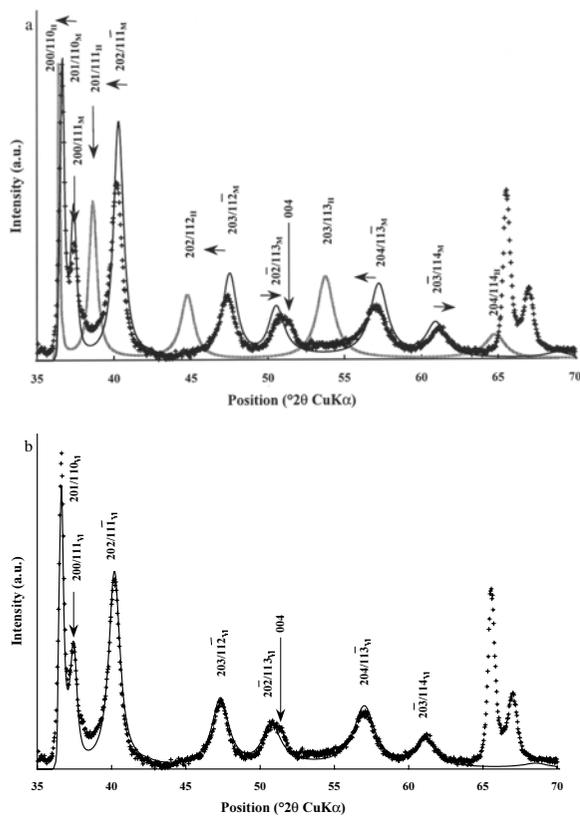
FIGURE 3. Comparison between experimental and calculated XRD patterns for ZnBi 122. (**a**) Patterns as for Figure 2 except for the gray line, which represents the XRD pattern calculated for the initial layer model of ZnBi 122 with a 1H layer stacking mode. Experimental reflections are located between calculated 20l,11l_M and 20l,11l_H reflections (M and H subscripts refer to the 1M and 1H initial models of ZnBi 122, successive layers being shifted with respect to each other by +**a**/3 in the 1M phase). Horizontal arrows indicate the shift of experimental 20l,11l reflections from the positions of 20l,11l_M reflections calculated for the defect-free 1M model. (**b**) Defective 1M ZnBi model containing 12% of orthogonal layer pairs.

FIGURE 4. Comparison between experimental and calculated XRD patterns for CdBi 106 (top) and difference plots (bottom). Patterns as for Figure 2. Only 20l and 11l reflections are calculated. Atomic coordinates and other structural parameters used for the calculations are listed in Tables 2, 4, 5, and 6. (**a**) Defect-free (no well-defined stacking faults) 1H CdBi model. Positions of calculated 201,111$_H$ and 202,112$_H$ reflections are slightly shifted toward lower 2θ values with respect to the corresponding experimental reflections (arrows). (**b**) Defective 1H CdBi model containing 7% of monoclinic layer pairs (+**a**/3 shift between adjacent layers, Table 4).

and 203,11$\overline{2}_M$, respectively, that is, toward higher 2θ values as needed to fill the gap between experimental and calculated peak positions. The best agreement between these peak positions was obtained for a defective 1H CdBi model containing 8% of monoclinic layer pairs (Fig. 4b, R_{WP} = 9.6%). For PbBi 6 and 58, calculation of XRD patterns shows that the amount of monoclinic layer pairs does not exceed 2–3%. The proportions of random and well-defined stacking faults providing the best agreement between experimental and calculated XRD patterns are listed in Table 4, as well as the optimum sizes of coherent scattering domains for each sample. One may note in this Table that, in addition to the well-defined stacking faults, all samples contain a significant amount of random stacking faults (12–19%, Table 4).

Optimal structural parameters for 1H samples

Even though XRD patterns calculated for the initial 1H models of PbBi 6, 58 and CdBi 106 reproduce reasonably well
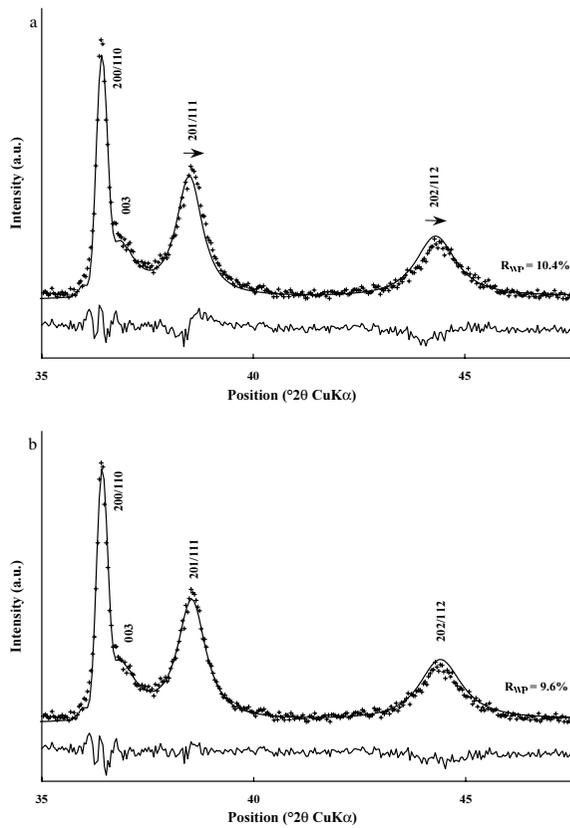
their main diffraction features, several structural parameters were varied to improve the agreement between experimental and calculated patterns. Because of the high sensitivity of the intensity distribution to the amount of Mn and interlayer Me, these parameters were analyzed with special care, and it was found that their optimal values matched those set in the initial models on the basis of chemical analyses (Tables 1, 5). Additional structural parameters such as the number of vacant layer sites and the positions and content of H_2O molecules coordinated (or not) to interlayer cations were adjusted. In particular, it was assumed initially that H_2O_{Me} formed regular triangles with edge lengths equal to the b parameter, but this assumption led to short distances between H_2O_{Me} and O_{layer} of the next layer (H-bonds). This structural inconsistency was solved by shifting these H_2O_{Me} in the **a-b** plane, their z-coordinate being adjusted to maintain realistic H_2O_{Me}-Me distances.

The experimental XRD pattern of PbBi 6 was reproduced best by keeping the structural parameters of the initial model,

and by adjusting the Pb z-coordinate and the x-, y-, and z-coordinates of H_2O_{Pb} (Tables 2, 4, 5, and 6a; Fig. 5; R_{WP} = 10.0%, R_{EXP} = 3.4%). As a result of the shift in the **a-b** plane of H_2O_{Pb} from the initial anion close-packing position (Fig. 6a), Pb has a distorted octahedral coordination. The H_2O_{Pb}-H_2O_{Pb} distance is increased up to 4.05 Å whereas the O_{layer}-O_{layer} distance is 2.84 Å (Fig. 6a). Lead octahedra are also flattened, as the difference between Pb and H_2O_{Pb} coordinates in projection on the **c** axis (1.12 Å) is smaller than that between Pb and O_{layer} coordinates (1.54 Å, Table 6a; Fig. 6b); in parallel, Pb-O_{layer} interatomic distances (2.25 Å) are shorter than Pb-H_2O_{Pb} distances (2.59 Å, Table 7). As a result of the displacement of H_2O_{Pb} in the **a-b** plane, the H_2O_{Pb}-O_{layer} distances increase from 2.15 Å in the initial model up to 2.66 Å, a sound value for the formation of strong H-bonds (Table 7; Fig. 6b).

The experimental XRD pattern of PbBi 58 differs significantly from that calculated for the initial model 1 in which all Pb atoms (0.056 atoms per octahedron) are located above or below layer vacant octahedra (Table 1, Fig. 7a; R_{WP} = 10.1%).
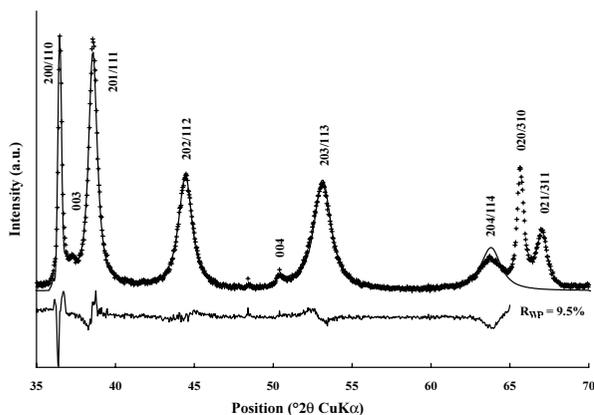
FIGURE 5. Comparison between experimental and calculated XRD patterns for PbBi 6 (top) and difference plot (bottom). Patterns as for Figure 2. Only 20*l* and 11*l* reflections are calculated. Atomic coordinates and other structural parameters used for the calculations are listed in Tables 2, 4, 5, and 6a. Optimum model.

TABLE 4. Optimum structural parameters used for the simulation of X-ray diffraction profiles

Sample	Well-defined faults		Wr Abund.	Radius (Å)	Mean N	Max N
	Prop.	Displ.				
ZnBi 122	12%	no shift	12%	300	7	35
ZnBi 128	15%	no shift	15%	225	7	35
PbBi 6	2%	−**a**/3	15%	175	6	30
PbBi 58	3%	−**a**/3	19%	200	5	25
CdBi 106	8%	+**a**/3	14%	160	6	30

Notes: Parameters defining layer stacking mode. Optimal values were determined by trial-and-error fitting of the experimental XRD patterns (Figs. 5, 7b, 9, and 11b). Proportions of well-defined stacking faults represented by 1M (±**a**/3) and 1H (no shift between adjacent layers) layer pairs are given for 1H and 1M varieties, respectively. Wr is the proportion of random stacking faults. The radius of the coherent scattering domains is given in the **a-b** plane, whereas the coherent scattering domain along the **c***-axis is noted N and is expressed as a number of layers.
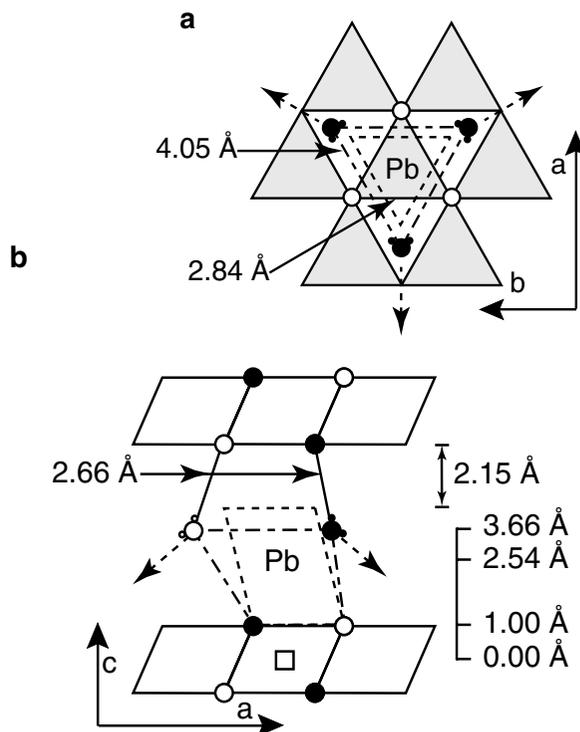
FIGURE 6. Schematic view of Pb site above/below vacant layer octahedra (^{VI}TC site). (x, y) coordinates of this position are (0, 0). (**a**) Projection on the **a-b** plane. The upper surface of the lower layer is shown as light shaded triangles. O_{layer} of this lower layer is shown as open circles. Dashed line outlines the ideal octahedron defined by the close packing of anions whereas irregular dashed line outlines the actual upper surface of the Pb octahedron, after further adjustment (arrows) of H_2O positions to obtain realistic Pb-$H_2O_{interlayer}$ and $H_2O_{interlayer}$-O_{layer} distances. (**b**) Projection along the **b** axis. O_{layer} is shown as large circles. Open symbols indicate atoms at y = 0, and solid symbols indicate atoms at y = ±1/2. Vacant layer sites are shown as open squares and Mn_{layer} is not shown. Other patterns as Figure 6a. Z-coordinates of Mn_{layer}, O_{layer}, Pb, and $H_2O_{interlayer}$ are indicated.

Because SAED results suggest the presence of Pb located above/below empty tridentate cavities in some PbBi 58 crystals (Drits et al. 2002), this additional interlayer position, whose symbolic notation is AbC$_{a'B'}$ $^{B'c'}$AbC, was considered. In this position, Pb shares three edges with underlying Mn_{layer} octahedra forming a triple edge-sharing surface complex (^{VI}TE site, Fig. 8; Spadini et al. 1994), as in quenselite (PbMnO$_2$OH, Rouse 1971). Adding this interlayer position and constraining the overall interlayer composition to chemical analysis yielded an optimal fit to the data (0.112 $Mn_{interlayer}$ in ^{VI}TC sites, 0.044 and 0.010 Pb in ^{VI}TC, and ^{VI}TE sites, respectively; Fig. 7b; Tables 1, 5, 6b, and 7; R_{WP} = 9.2%, R_{EXP} = 3.1%). One can note that a fit similar to the one described may be obtained (Fig. 7c; R_{WP} = 9.1%) with a slightly different interlayer composition (0.123 $Mn_{interlayer}$, 0.044 Pb in ^{VI}TC sites, and 0.010 Pb in ^{VI}TE sites) in which the amount of interlayer cations located in ^{VI}TC sites only is equal to the amount of vacant layer sites (0.167 per octahedron). In both cases, the size and shape of ^{VI}TC sites are similar to those

TABLE 5. Optimum structural parameters used for the simulation of X-ray diffraction profiles

Sample	Vacancies	(Mn + Me)$_{inter.}$	Me/Mn	H$_2$O/Mn	H$_2$O coord. Me/Me	Add. H$_2$O + Na
ZnBi 122	0.167	0.216	0.127	0.294/0.098	0.234/0.078	0.180
					0.040/0.040	
ZnBi 128	0.167	0.224	0.133	0.300/0.100	0.252/0.084	0.150
					0.040/0.040	
PbBi 6	0.167	0.166	0.008	0.480/0.160	0.024/0.008	0.280
PbBi 58	0.167	0.166	0.057	0.336/0.112	0.132/0.044	0.500
					0.030/0.010	
CdBi 106	0.167	0.220	0.121	0.324/0.108	0.342/0.114	0.180

Notes: Parameters defining the layer cation composition. Optimal values have been determined by trial-and-error fitting of the experimental XRD patterns (Figs. 5, 7b, 9, and 11b). When two amounts are given for H$_2$O$_{interlayer}$ coordinating Me, the upper one refers to Me in ^{VI}TC sites, whereas the lower one refers to Me in ^{IV}TC (Zn) or ^{VI}TE (Pb) sites.
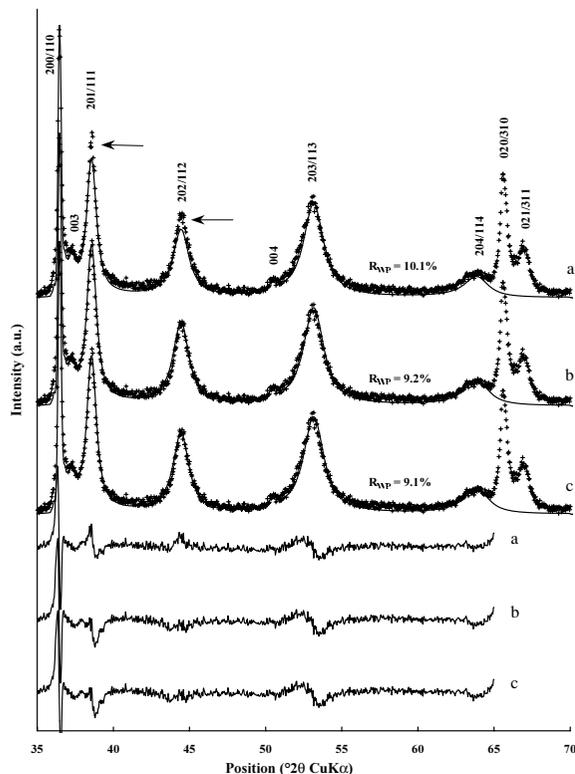

FIGURE 7. Comparison between experimental and calculated XRD patterns for PbBi 58 (top) and difference plots (bottom). Patterns as for Figure 2. Only 20l and 11l reflections are calculated. Atomic coordinates and other structural parameters used for the calculations are listed in Tables 2, 4, 5, and 6b. (**a**) Initial model in which all Mn$_{interlayer}$ (0.112 per octahedron) and Pb (0.054 per octahedron) are located only above or below vacant layer sites (^{VI}TC sites). (**b**) Optimum model, with 0.044 and 0.010 Pb located in ^{VI}TC and ^{VI}TE sites, respectively. (**c**) Model in which the amount of Mn$_{interlayer}$ is increased to 0.123, as compared with the optimum 0.112 value. Distribution of Pb is similar to that of the optimal model.

described for PbBi6 (Fig. 6), whereas ^{VI}TE sites are less distorted (Fig. 8). In comparison with the Pb ^{VI}TC octahedra, the flattening of the ^{VI}TE octahedra is reduced, as differences between Pb and H$_2$O$_{Pb}$ coordinates in projection on the **c** axis are increased (1.42 vs 1.12 Å). As a result, H$_2$O$_{Pb}$-H$_2$O$_{Pb}$ distances (3.77 Å) are also shorter than those in ^{VI}TC octahedra (4.06 Å). In these two octahedral sites, the distance between H$_2$O$_{Pb}$ and
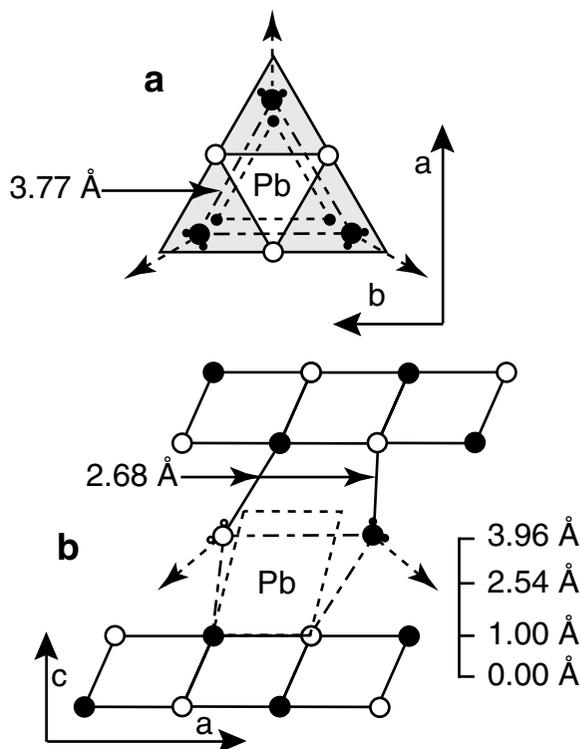

FIGURE 8. Schematic view of Pb site above/below empty tridentate cavities (^{VI}TE site). (x, y) coordinates of this position are (–0.333, 0) above the lower layer and (0.333, 0) below this layer. All patterns as for Fig. 6. (**a**) Projection on the **a-b** plane. Small solid circles represent Mn$_{layer}$ from the lower layer. (**b**) Projection along the **b** axis.

O$_{layer}$ of the next layer (2.65–2.68 Å) allows the formation of strong H-bonds.

The Cd z-coordinate and the x-, y-, and z-coordinates of H$_2$O$_{Cd}$ in CdBi 106 had to be adjusted from the initial model to obtain an optimal agreement between experimental and calculated XRD patterns (Tables 5, 6c; Fig. 9; R_{WP} = 8.4%, R_{EXP} = 4.1%). The optimal amounts of Cd (0.114) and Mn$_{interlayer}$ (0.108) are close to those derived from chemical analysis (0.100 and 0.116, respectively; Tables 1 and 5). In projection on the **c** axis, Cd is located halfway from H$_2$O$_{Cd}$ and bound O$_{layer}$, but Cd-O$_{layer}$ distances (2.10 Å) are shorter than Cd-H$_2$O$_{Cd}$ distances (2.35 Å) because H$_2$O$_{Cd}$ was shifted in the **a-b** plane from its ideal anion close-packing position. As a result of this shift, H$_2$O$_{Cd}$-H$_2$O$_{Cd}$ dis-
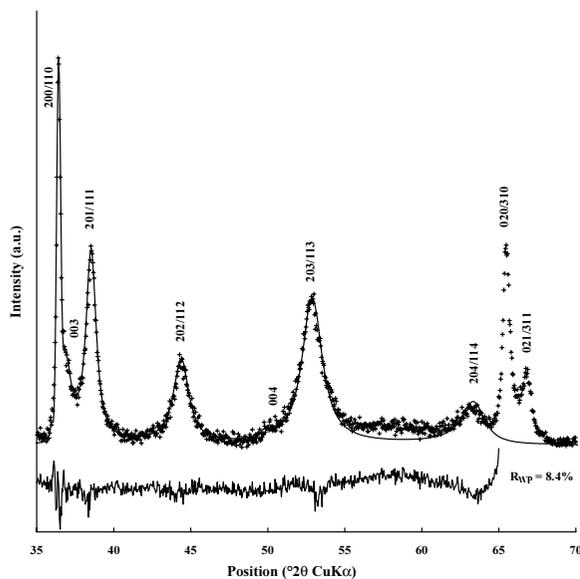
FIGURE 9. Comparison between experimental and calculated XRD patterns for CdBi 106 (top) and difference plot (bottom). Optimum model. Patterns as for Figure 2. Only 20*l* and 11*l* reflections are calculated. Atomic coordinates and other structural parameters used for the calculations are listed in Tables 2, 4, 5, and 6c.

tances are equal to 3.37 Å, whereas distances between H_2O_{Cd} and O_{layer} of the next layer are equal to 2.68 Å, thus allowing the formation of strong H-bonds.

Optimal structural parameters for 1M samples

In contrast to the previous models, no adjustment of the amount of $Mn_{interlayer}$ and Me from their initial values (Table 1) could provide a satisfactory fit to the experimental XRD patterns. Indeed, calculated $20\bar{l},11(l+1)$, and $20l,11(\bar{l}-1)$ reflection intensities ($l \leq 3$) are much stronger than experimental ones when all interlayer cations (0.094 $Mn_{interlayer}$ and 0.116 Zn, Table 5) have octahedral coordination (Fig. 11a; $R_{WP} = 14.9\%$). Because the coexistence of octahedrally (^{VI}Zn) and tetrahedrally (^{IV}Zn) coordinated Zn TC surface complexes was established in these samples from EXAFS spectroscopy (Manceau et al. 2002), the additional presence of ^{IV}Zn was introduced in the XRD simulations. Such a mixed tetrahedral and octahedral Zn coordination is common and has been described in a number of structures including hydrozincites—$Zn_5(OH)_6(CO_3)_2$ and $Zn_5(OH)_8(NO_3)_2(H_2O)_2$ (Ghose 1964; Stählin and Oswald 1970), becthererite—$Zn_7Cu(OH)_{13}[SiO(OH)_3SO_4]$ (Hoffman et al. 1997), mooreite—$(Mg, Zn, Mn)_{15}(SO_4)_2(OH)_{26}.8H_2O$ (Hill 1980), torreyite—$(Mn, Mg)_9Zn_4(SO_4)_2(OH)_{22}.8H_2O$ (Treiman and Peacor 1982), and synthetic $Zn_5(OH)_8Cl_2H_2O$ (Allman 1969). These solids exhibit similar structures, with ^{VI}Zn building up a brucite-like layer and octahedral layer vacancies capped by ^{IV}Zn in the interlayer. In order to assess the sensitivity of XRD to the position of ^{IV}Zn, two alternative structural models were considered. In the first, ^{IV}Zn is located either above or below vacant layer sites (^{IV}TC site; Fig. 10a), and the idealized local 1M ZnBi structure may be represented as:
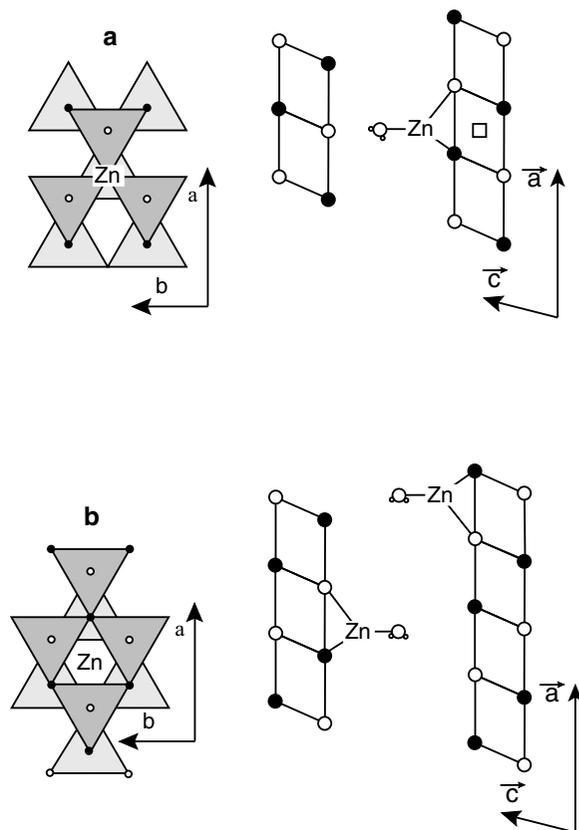

FIGURE 10. Possible positions of ^{IV}Zn in the interlayer space of ZnBi. Adjacent layers are translated by $c\cdot\cos\beta = +0.333$ a along the **a** axis. In projection on the **a-b** plane (left), small circles represent Mn_{layer} from the lower (solid circles) and upper (open circles) layers defining the interlayer space. The upper surface of the lower layer and the lower surface of the upper layer are shown as light and dark shaded triangles, respectively. O_{layer} are not shown. In projection along the **b** axis (right), patterns as for Figure 6b. (**a**) ^{IV}Zn is located above/below vacant layer sites. (x, y) coordinates of this position are (0, 0) for the lower layer (^{IV}TC site). (**b**) ^{IV}Zn is located above/below empty tridentate cavities. (x, y) coordinates of this position are (–0.333, 0) above the lower layer and (0.333, 0) below this layer (^{IV}TE site).

$$AbC_{b'B'}{}^{C'c'}BcA_{c'C'}{}^{A'a'}CaB_{a'A'}{}^{B'b'}AbC\ldots \quad (7)$$
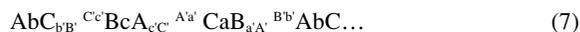
where a', b', and c' are the ^{IV}Zn sites, A', B', and C' the sites for H_2O_{Zn} which are located just above or below O_{layer} (A, B, and C sites; Fig. 10a). In the alternative model, ^{IV}Zn forms a TE complex as Pb in PbBi 58 (Fig. 10b). Its distribution in ZnBi interlayers may be described locally as :

$$AbC_{a'A'}{}^{A'a'}BcA_{b'B'}{}^{B'b'}CaB_{c'C'}{}^{C'c'}AbC\ldots \quad (8)$$
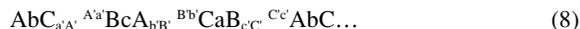
The best possible agreement between experimental and calculated XRD profiles (Fig. 11b; $R_{WP} = 10.3\%$, $R_{EXP} = 3.5\%$) was obtained for a model in which 0.098 $Mn_{interlayer}$ and 0.078 Zn per octahedron are octahedrally coordinated at TC sites and

TABLE 6A. Optimum structural parameters used for the simulation of PbBi 6 X-ray diffraction profile (Fig. 5)

Atom	x	y	ζ	Occ.	x	y	ζ	Occ.
Mn$_{layer}$	0	0	0	0.833	–	–	–	–
O$_{layer}$	0.333	0	1.00	1	–0.333	0	–1.00	1
Mn$_{interlayer}$	0	0	2.04	0.080	0	0	–2.04	0.080
H$_2$O$_{inter.}$	–0.333	0	3.13	0.240	0.333	0	–3.13	0.240
Pb	0	0	2.54	0.004	0	0	–2.54	0.004
in TC sites
H$_2$O$_{inter.}$	–0.475	0	3.66	0.004	0.475	0	–3.66	0.004
H$_2$O$_{inter.}$	0.238	0.713	3.66	0.004	–0.238	0.713	–3.66	0.004
H$_2$O$_{inter.}$	0.238	–0.713	3.66	0.004	–0.238	–0.713	–3.66	0.004
H$_2$O$_{inter.}$	–0.333	0	3.614	0.28	–	–	–	–
and Na$_{inter.}$ Add. Pos.

Notes: Optimal values were determined by trial-and-error fitting of the experimental XRD patterns. x, and y coordinates are expressed as fractions of the a and b parameters, respectively. Coordinates along the **c*** axis, ζ, are expressed in Å to emphasize the thickness of layer and interlayer polyhedra.

TABLE 6B. Optimum structural parameters used for the simulation of PbBi 58 X-ray diffraction profile (Fig. 7b)

Atom	x	y	ζ	Occ.	x	y	ζ	Occ.
Mn$_{layer}$	0	0	0	0.833	–	–	–	–
O$_{layer}$	0.333	0	1.00	1	–0.333	0	–1.00	1
Mn$_{interlayer}$	0	0	2.04	0.056	0	0	–2.04	0.056
H$_2$O$_{inter.}$	–0.333	0	3.13	0.168	0.333	0	–3.13	0.168
Pb	0	0	2.54	0.022	0	0	–2.54	0.022
in TC sites
H$_2$O$_{inter.}$	–0.475	0	3.66	0.022	0.475	0	–3.66	0.022
H$_2$O$_{inter.}$	0.238	0.713	3.66	0.022	–0.238	0.713	–3.66	0.022
H$_2$O$_{inter.}$	0.238	–0.713	3.66	0.022	–0.238	–0.713	–3.66	0.022
Pb	–0.333	0	2.54	0.005	0.333	0	–2.54	0.005
in TE sites
H$_2$O$_{inter.}$	0.109	0	3.96	0.005	–0.109	0	–3.96	0.005
H$_2$O$_{inter.}$	–0.554	0.663	3.96	0.005	0.554	0.663	–3.96	0.005
H$_2$O$_{inter.}$	–0.554	–0.663	3.96	0.005	0.554	–0.663	–3.96	0.005
H$_2$O$_{inter.}$	–0.333	0	3.609	0.50	–	–	–	–
and Na$_{inter.}$ Add. Pos.

TABLE 6C. Optimum structural parameters used for the simulation of CdBi 106 X-ray diffraction profile (Fig. 9)

Atom	x	y	ζ	Occ.	x	y	ζ	Occ.
Mn$_{layer}$	0	0	0	0.833	–	–	–	–
O$_{layer}$	0.333	0	1.00	1	–0.333	0	–1.00	1
Mn$_{interlayer}$	0	0	2.04	0.054	0	0	–2.04	0.054
H$_2$O$_{inter.}$	–0.333	0	3.13	0.162	0.333	0	–3.13	0.162
Cd	0	0	2.31	0.057	0	0	–2.31	0.057
in TC sites
H$_2$O$_{inter.}$	–0.394	0	3.62	0.057	0.394	0	–3.62	0.057
H$_2$O$_{inter.}$	0.197	0.591	3.62	0.057	–0.197	0.591	–3.62	0.057
H$_2$O$_{inter.}$	0.197	–0.591	3.62	0.057	–0.197	–0.591	–3.62	0.057
H$_2$O$_{inter.}$	–0.333	0	3.644	0.18	–	–	–	–
and Na$_{inter.}$ Add. Pos.

TABLE 6D. Optimum structural parameters used for the simulation of ZnBi 122 X-ray diffraction profile (Fig. 11b)

Atom	x	y	z	Occ.	x	y	z	Occ.
Mn$_{layer}$	0	0	0	0.833	–	–	–	–
O$_{layer}$	0.333	0	1.00	1	–0.333	0	–1.00	1
Mn$_{interlayer}$	0	0	2.04	0.049	0	0	–2.04	0.049
H$_2$O$_{inter.}$	–0.333	0	3.13	0.147	0.333	0	–3.13	0.147
Zn	0	0	2.21	0.039	0	0	–2.21	0.039
in ^{VI}TC sites
H$_2$O$_{inter.}$	–0.333	0	3.55	0.117	0.333	0	–3.55	0.117
Zn	0	0	1.77	0.020	0	0	–1.77	0.020
in ^{IV}TC sites
H$_2$O$_{inter.}$	0	0	3.70	0.020	0	0	–3.70	0.020
H$_2$O$_{inter.}$	–0.333	0	3.535	0.18	–	–	–	–
and Na$_{inter.}$ Add. Pos.

TABLE 6E. Optimum structural parameters used for the simulation of ZnBi 122 X-ray diffraction profile

Atom	x	y	ζ	Occ.	x	y	ζ	Occ.
Mn$_{layer}$	0	0	0	0.833	–	–	–	–
O$_{layer}$	0.333	0	1.00	1	–0.333	0	–1.00	1
Mn$_{interlayer}$	0	0	2.04	0.050	0	0	–2.04	0.050
H$_2$O$_{inter.}$	–0.333	0	3.13	0.150	0.333	0	–3.13	0.150
Zn in	0	0	2.21	0.042	0	0	–2.21	0.042
^{VI}TC sites
H$_2$O$_{inter.}$	–0.333	0	3.55	0.126	0.333	0	–3.55	0.126
Zn in	0	0	1.77	0.020	0	0	–1.77	0.020
^{IV}TC sites
H$_2$O$_{inter.}$	0	0	3.70	0.020	0	0	–3.70	0.020
H$_2$O$_{inter.}$	–0.333	0	3.535	0.15	–	–	–	–
and Na$_{inter.}$ Add. Pos.

TABLE 7. Typical inter-atomic distances calculated from the optimum atomic coordinates

Sample	Mn$_{layer}$-O$_{layer}$	Mn$_{inter.}$-O$_{layer}$	Mn$_{inter.}$-H$_2$O	Me$_{inter.}$-O$_{layer}$	Me$_{inter.}$-H$_2$O	H$_2$O$_{inter}$-O$_{layer}$	Me$_{inter.}$-Mn$_{layer}$
ZnBi 122	1.925	1.946	1.973	2.04 (^{VI}TC site)	2.12 (^{VI}TC site)	3.01 (^{VI}TC site)	3.60 (^{VI}TC site)
				1.81* (^{IV}TC site)	1.93 (^{IV}TC site)	2.37† (^{IV}TC site)	3.35 (^{IV}TC site)
ZnBi 128	1.923	1.944	1.972	2.04 (^{VI}TC site)	2.12 (^{VI}TC site)	3.01 (^{VI}TC site)	3.60 (^{VI}TC site)
				1.92 (^{IV}TC site)	1.60[1] (^{IV}TC site)	2.37[1] (^{IV}TC site)	3.48 (^{IV}TC site)
PbBi 6	1.923	1.944	1.971	2.25	2.59[2]	2.66[2]	3.81
PbBi 58	1.923	1.944	1.971	2.25 (^{VI}TC site)	2.59 (^{VI}TC site)	2.65[2] (^{VI}TC site)	3.81 (^{VI}TC site)
				2.25 (^{VI}TE site)	2.60 (^{VI}TE site)	2.68 (^{VI}TE site)	3.02 (^{IV}TE site)
CdBi 106	1.925	1.946	1.973	2.10	2.35	2.68	3.66

Note: All distances are given in Å.
* Indicates a very short distance which may be increased by a shift of Zn from its ideal position either in the **ab** plane or along the **c*** axis.
† Indicates a very short distance which may be increased by additional displacement of interlayer H$_2$O molecules (Fig. 13a).

0.040 Zn atoms are tetrahedrally coordinated at ^{IV}TC sites, in agreement with EXAFS results (Manceau et al. 2002). The z-coordinate for ^{IV}Zn was calculated from the ^{IV}Zn-nearest Mn$_{layer}$ EXAFS distance (3.35 Å; Manceau et al. 2002) using the following equation:

$$z(\mathrm{Zn}) = \sqrt{d_{(\mathrm{Zn-Mn})}^2 - b^2} = \sqrt{3.35^2 - 2.846^2} = 1.77 \text{ Å}$$

In turn, the z-coordinate of H$_2$O$_{Zn}$ was set to: $z(\mathrm{H_2O}) = z(\mathrm{Zn}) + d_{(\mathrm{Zn-H_2O})} = 3.70$ Å, assuming that $d_{(\mathrm{Zn-H_2O})} = 1.93$ Å.

To illustrate the sensitivity of XRD patterns to the location of ^{IV}Zn, an XRD profile (Fig. 11c; $R_{WP} = 26.2\%$) was calculated for a model with the same interlayer cation composition (0.098 ^{VI}Mn$_{interlayer}$, 0.078 ^{VI}Zn, and 0.040 ^{IV}Zn per octahedron) as that used for the optimum fit but with Zn located in the alternative ^{IV}TE site (Fig. 10b).

The same approach was applied to ZnBi 128 and led to a 0.100 ^{VI}Mn$_{interlayer}$, 0.084 ^{VI}Zn, and 0.040 ^{IV}Zn cation interlayer composition, all cations being located in TC sites. Optimal parameters for the two ZnBi varieties are listed in Tables 2, 4, 5, and 6d,e.
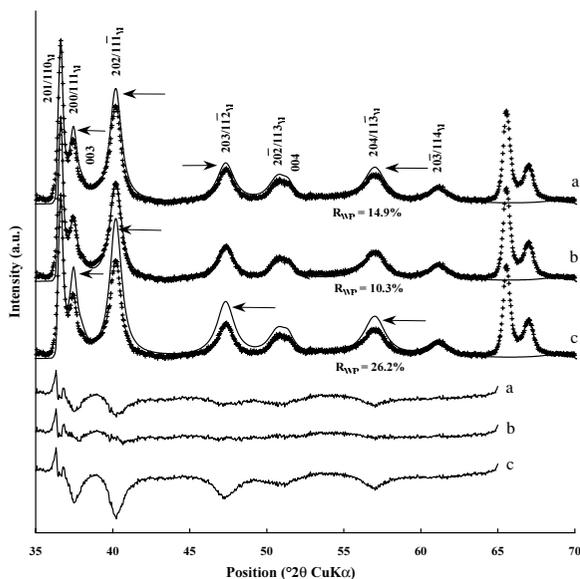
FIGURE 11. Comparison between experimental and calculated XRD patterns for ZnBi 122 (top) and difference plots (bottom). Patterns as for Figure 2. Only $20l$ and $11l$ reflections are calculated. Atomic coordinates and other structural parameters used for the calculations are listed in Tables 2, 4, 5, and 6d. (**a**) All Zn cations (0.116 per octahedron) are octahedrally coordinated as compared with the optimum 0.078:0.040 ratio between octahedrally and tetrahedrally coordinated Zn. (**b**) Optimum model. (**c**) Tetrahedrally coordinated Zn (0.040 per octahedron) is located above/below empty tridentate cavities (Fig. 10b), rather above/below vacant layer sites (Fig. 10a).

DISCUSSION

Layer stacking mode in MeBi as a function of the nature and structure of Me complex

The layer stacking mode in MeBi depends on the nature of cations sorbed from solution, as illustrated by the 1H structure of PbBi and CdBi and the 1M structure of ZnBi. In these structures, interlayer cations are uniquely (Cd, Zn) or predominantly (Pb) located above/below vacant layer sites, as 25% of total Pb cations are located above and/or below empty tridentate cavities (^{VI}TE sites) in sample PbBi 58. In addition, about 30% of total Zn cations are tetrahedrally coordinated in ZnBi. To understand the reason for the formation of 1H or 1M MeBi from the initial NaBu, the interlayer structures of these two types of low-pH birnessite must be compared.

In the 1H structure (Fig. 12a), the distance between Me in ^{VI}TC sites and the nearest Mn_{layer} of the adjacent layer is short (4.7–5.0 Å). In addition, their electrostatic repulsion is not screened by anions, as the three H_2O_{Me} form a distorted empty prism with the three closest O_{layer} of the adjacent layer. In contrast, the location of Me in TE sites prevents such a direct electrostatic interaction with Mn_{layer} of the adjacent layer (Fig. 8). Because $H_2O_{interlayer}$-O_{layer} distances are similar for both interlayer configurations (2.65–2.68 Å; Table 7), either location of Pb provides an equal opportunity for the formation of strong H-bonds between O_{layer} of one layer and H_2O_{Me} of the adjacent
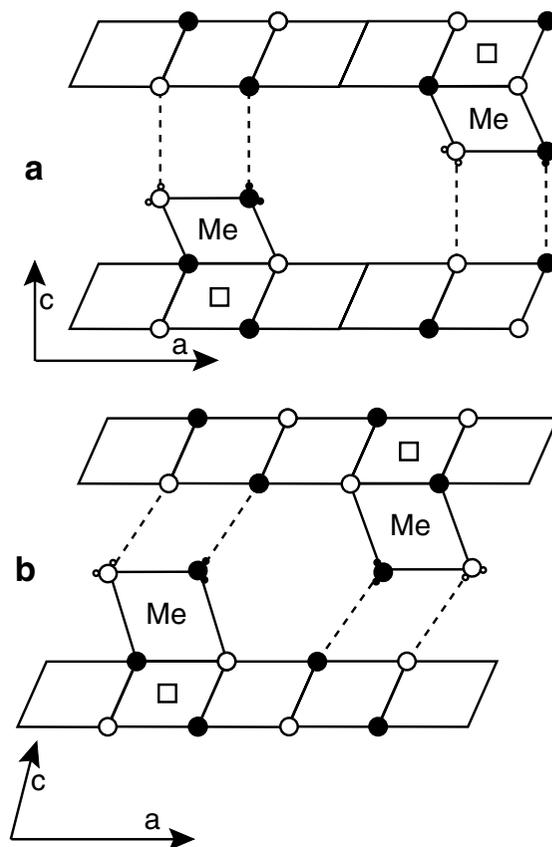

FIGURE 12. Projection of the layer and interlayer structures of the MeBi structures along the **b** axis (modified from Lanson et al. 2000). Oxygen atoms are shown as large circles. Vacant layer sites are shown as open squares. Saturated O_{layer} and protons are not shown. Open symbols indicate atoms at $y = 0$, and solid symbols indicate atoms at $y = \pm^1/_2$. Bonds between very undersaturated O_{layer} and H_2O_{Me} are outlined by dashed lines. These dashed lines also indicate possible H-bonds between these two species. (**a**) Idealized structural model for the 1H phase of MeBi. (**b**) Idealized structural model for the 1M phase of MeBi. The edges of the octahedra defined by very undersaturated O_{layer} and H_2O_{Me} are too long to permit H-bonds.

one. The essential control exerted by these H-bonds on the layer stacking mode is evidenced by the prevalence of the 1H HBi phase at low pH (Lanson et al. 2000). Predominance of Pb in ^{VI}TC sites is likely related to the formation of vacant layer octahedra during the NaBu-to-PbBi transformation, as location of Pb above and/or below these sites provides better local charge compensation than location of Pb in ^{VI}TE sites, the latter sharing only one edge with vacant octahedra.

In contrast to the 1H MeBi phase, distances between Mn_{layer} and Me from adjacent layers are maximized in the 1M structure (Fig. 12b), which minimizes the electrostatic repulsion between these cations. However, H_2O_{Me} molecules form an empty octahedron with O_{layer} atoms of the adjacent layer (Fig. 12b) and, accordingly, the H_2O_{Zn}-O_{layer} distance in 1M ZnBi (~3.0 Å) is much longer than in the 1H structure, resulting in much weaker H-bonds as in the 1M HBi structure described by

Lanson et al. (2000). Interestingly, the ^{IV}Zn complex serves to stabilize the 1M structure as H_2O_{Zn} coordinating ^{IV}Zn is located just above or below O_{layer} of the adjacent layer (Fig. 10a). The resulting O_{layer}-H_2O_{Zn} distance (2.37 Å; Table 7) is short, but plausible, and may always be increased by shifting H_2O_{Zn} in the **a-b** plane to form an obtuse Zn-H_2O_{Zn}-O_{layer} angle (Fig. 13). Thus, despite the +**a**/3 displacement between adjacent layers, which is *a priori* unfavorable to the formation of strong H-bonds between layers, the tetrahedral coordination of Zn offers this opportunity.

Structural formulae and crystal-chemical features of MeBi

According to Lanson et al. (2000), the structural formula of synthetic HBi prepared at pH 4 is $H_{0.320}^+Mn_{0.123}^{3+}Mn_{0.043}^{2+}$ $(Mn_{0.722}^{4+}Mn_{0.111}^{3+}\square_{0.167})O_2 \cdot 0.487H_2O$. Because the amount of vacant layer sites in all studied MeBi samples (0.167 per octahedron) is identical to that of HBi prepared at different pHs (5–2), it is logical to assume that the disproportionation and migration reactions occurring during the NaBu-to-MeBi transformation are similar to those described for the NaBu-to-HBi transformation by Drits et al. (1997), Silvester et al. (1997), and Lanson et al. (2000). As a consequence, layer cation composition, and especially the relative proportions of heterovalent Mn cations, are assumed to be identical in all MeBi samples. As a result, the following structural formulae were calculated from the content of $Mn_{interlayer}$, Me, and H_2O determined from the simulation of XRD patterns (Table 5), and from the Na content determined by chemical analysis (Table 1): $H_{0.23}^+Na_{0.092}^+Mn_{0.123}^{3+}Mn_{0.037}^{2+}Pb_{0.006}^{2+}(Mn_{0.722}^{4+}$ $Mn_{0.111}^{3+}\square_{0.167})O_2 \cdot 0.77H_2O$ (PbBi 6), $H_{0.24}^+Na_{0.063}^+Mn_{0.123}^{3+}{}^{TE}Pb_{0.010}^{2+}$ $^{TC}Pb_{0.044}^{2+}(Mn_{0.722}^{4+}Mn_{0.111}^{3+}\square_{0.167})O_2 \cdot 0.63H_2O$ (PbBi 58), $H_{0.23}^+$ $Mn_{0.108}^{3+}Cd_{0.114}^{2+}(Mn_{0.722}^{4+}Mn_{0.111}^{3+}\square_{0.167})O_2 \cdot 0.73H_2O$ (CdBi 106), $H_{0.25}^+Mn_{0.098}^{3+}{}^{VI}Zn_{0.078}^{2+}{}^{IV}Zn_{0.040}^{2+}(Mn_{0.722}^{4+}Mn_{0.111}^{3+}\square_{0.167})O_2 \cdot 0.74H_2O$ (ZnBi 122), $H_{0.23}^+Na_{0.02}^+Mn_{0.100}^{3+}{}^{VI}Zn_{0.084}^{2+}{}^{IV}Zn_{0.040}^{2+}(Mn_{0.722}^{4+}Mn_{0.111}^{3+}$ $\square_{0.167})O_2 \cdot 0.75H_2O$ (ZnBi 128).

Compared with HBi, MeBi samples contain a significantly lower amount of H^+, based on charge balance. Sodium is totally replaced by H^+ in the NaBu-to-HBi transformation, leading to the presence of 0.32 H^+ per octahedron (Lanson et al. 2000). It is very likely that the sorption of protons is significantly decreased by the presence of Me in solution because of its overwhelming concentration in solution.

The sum of $Mn_{interlayer}$ and ^{TC}Pb (0.166 per octahedron) in the two PbBi samples is similar to the amount of vacant layer sites (0.167 per octahedron), which suggest that these cations are located either above or below vacant layer sites in agreement with EXAFS results (Manceau et al. 2002). Conversely, in 1H CdBi and in 1M ZnBi, the sum of interlayer cations is significantly greater than 0.167 per octahedron. For these samples the difference between the amounts of vacant layer sites (0.167) and of $Mn_{interlayer}$ is systematically about half the amount of Me. Consequently, most Cd and Zn cations are likely located above and below the same vacant layer sites, whereas $Mn_{interlayer}^{3+}$ is located either above or below these sites. In addition, the amount of $Mn_{interlayer}$ in CdBi and ZnBi samples (0.098–0.108 atom per octahedron; Table 5) is similar to the amount of $Mn_{interlayer}^{3+}$ in 1H HBi (0.111 atoms per octahedron). The simi-
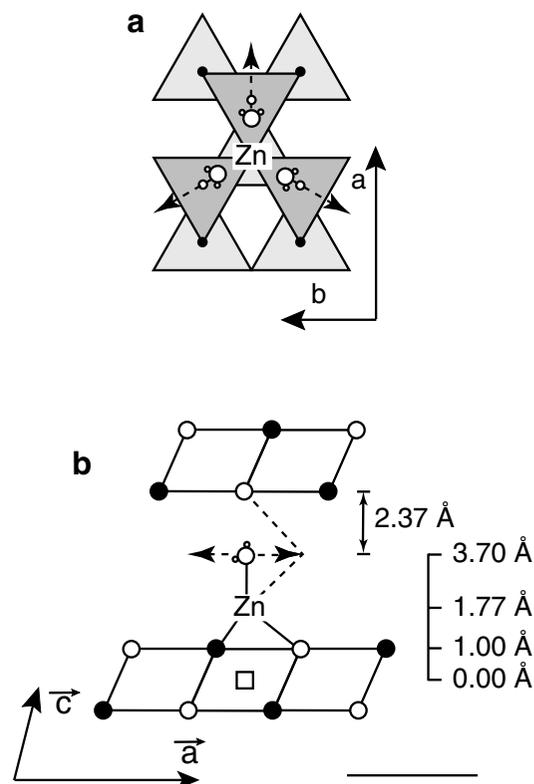

FIGURE 13. Schematic view of tetrahedrally coordinated Zn site vacant layer octahedra (^{VI}TC site). (x, y) coordinates of this position are (–0.333, 0) above the lower layer and (0.333, 0) below this layer. All patterns as for Figures 6 and 10. (**a**) Projection on the **a-b** plane. (**b**) Projection along the **b** axis. Dashed line outlines the obtuse Zn-$H_2O_{interlayer}$-O_{layer} angle resulting from the shift of $H_2O_{interlayer}$ in the **a-b** plane to increase the $H_2O_{interlayer}$-O_{layer} distance.

larity of the $Mn_{interlayer}$ contents suggest that during the NaBu transformation to CdBi and ZnBi, the main cation-exchange process occurs between interlayer Na and Mn^{2+}, leaving the solid, and Me and H^+, adsorbed from solution.

Layer charge compensation in MeBi

As mentioned before, all studied MeBi samples have the same layer cation composition and therefore the same high negative layer charge. As can be seen in Figure 14, O_{layer} atoms of a vacant octahedron ideally receive 0.500 + 0.667 = 1.167 positive charges if coordinated to Mn^{3+} and Mn^{4+} (half-filled circles), or 0.667 + 0.667 = 1.333 positive charges if coordinated to two Mn^{4+} (open circles). In both cases, these three O_{layer} are strongly undersaturated, as globally they receive only 4.000 (3 × 1.333; Fig. 14a), 3.833 (2 × 1.333 + 1.167; Fig. 14b), or 3.667 (2 × 1.167 + 1.333; Fig. 14c) positive charges, and therefore require two additional positive charges on each side of a vacant layer site to achieve local charge compensation. As a first approximation, charge balance is satisfied for CdBi and ZnBi as vacant layer sites are capped on both sides by Cd and Zn, respectively. This charge distribution
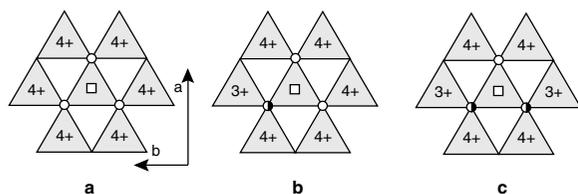
FIGURE 14. Idealized structure model for the MeBi phases. Distribution of undersaturated O_{layer} within the upper surface of the lower layer (grey triangles) in projection on the **ab**-plane. Mn^{3+}_{layer}, Mn^{4+}_{layer}, and vacant layer sites are shown as 3+, 4+, and open squares, respectively. Oxygen atoms forming the upper surface of the lower layer are shown as large circles. Saturated or almost saturated O_{layer} atoms are not shown, unsaturated O_{layer} atoms coordinated to 2 Mn^{4+}_{layer} are shown as open circles, whereas most undersaturated O_{layer} atoms coordinated to 1 Mn^{4+}_{layer}, and to 1 Mn^{3+}_{layer} are half-filled. Me is not shown.

is idealized as Zn and Cd share their charge between O_{layer} and H_2O_{Me} (Manceau et al. 2002). In turn, H_2O_{Me} transfers part of this positive charge to O_{layer} of the next layer through H-bonds. When a vacant layer site is capped by one $Mn^{3+}_{interlayer}$, local charge compensation requires the sorption of two protons on one side of this site and of $(Mn^{3+}OH^-)^{2+}$ on the other side. In this case, one H_2O molecule dissociates to permit this local charge compensation (Lanson et al. 2000). This second mechanism, which occurs in 1H HBi, may also exist in PbBi because interlayer cations are located either above or below vacant layer sites, as $Mn_{interlayer}$ in HBi.

In PbBi 58, local charge compensation is improved by the coexistence of ^{VI}Pb in both TC and TE sites on the two sides of a vacant layer octahedron. As an illustration, Figure 15 shows a PbBi layer fragment in which such a vacant octahedron shares edges with two Mn^{3+}- and four Mn^{4+}-octahedra leading to O_{layer} with contrasting degrees of undersaturation. As can be seen in this figure, location of Pb in both ^{VI}TE and ^{VI}TC sites optimally compensates the charge deficit of the most undersaturated O_{layer} (half-filled circles). Consistently, the interlayer cation compositions of 1H HBi (0.123 Mn^{3+}, 0.044 Mn^{2+}) and PbBi 58 (0.123 Mn^{3+}, 0.044 Pb^{2+} in ^{VI}TC sites and 0.010 Pb^{2+} in ^{VI}TE sites) suggest that during the NaBu-to-PbBi transformation $Mn^{2+}_{interlayer}$ is replaced by $Pb^{2+}_{interlayer}$, both cations being located in TC sites. Additional Pb likely locates in ^{VI}TE sites to compensate the negative charge of most undersaturated O_{layer}, and it probably migrates toward these atoms as described by Manceau et al. (2002).

From the above considerations, it is clear that, except for protons, interlayer monovalent cations cannot provide local charge compensation to the permanent charge of birnessite resulting from vacant layer sites. This conclusion is supported by the low amount of Na in MeBi, in spite of its high concentration in solution.

Structural heterogeneity of MeBi

As can be seen in Table 4, MeBi structural heterogeneity strongly depends on the nature of Me as, for example, Pb and Cd dramatically increase phase and structural homogeneity of MeBi as compared with HBi pH4. Indeed, HBi pH4 consists
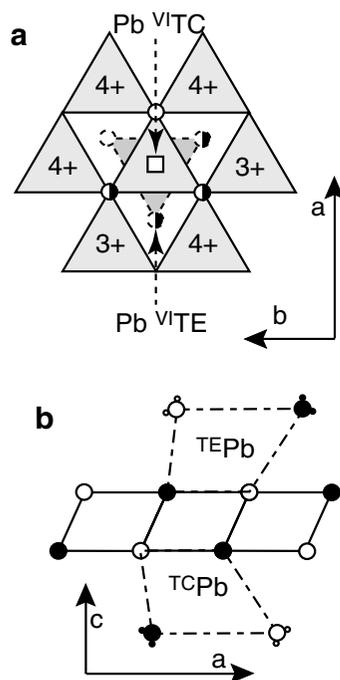

FIGURE 15. Idealized structure model for the PbBi 58 sample. (**a**) Projection on the **a-b** plane. All patterns as in Figure 14. The lower surface of the vacant layer site is shown as a dark shaded triangle outlined by a dashed line. O_{layer} atoms defining this surface are outlined by a dashed line. Pb is located below this vacancy in a ^{VI}TC site to compensate the two most undersaturated O_{layer}. Above this vacant site, Pb may equally be located in the ^{VI}TE site to compensate the two most undersaturated O_{layer} (half-filled circles). (**b**) Projection along the **b** axis. All patterns as in Figure 8b.

of a physical mixture of a 1H phase containing 15% of monoclinic layers pairs and of a 1M phase containing 40% of orthogonal layer pairs (Lanson et al. 2000). In contrast, the NaBu-to-PbBi transformation leads to the formation of unique 1H PbBi varieties containing only 2–3% of monoclinic layer pairs, even if the amount of Pb is low. A similar low content of monoclinic layer pairs (7%) was observed for the 1H CdBi phase.

The origin of MeBi structural homogeneity may be explained in light of the results obtained for low-pH HBi (Lanson et al. 2000). These authors showed that almost defect-free 1H HBi is formed either when a sufficiently slow reaction rate permits additional ±a/3 adjustments of adjacent layers leading to a defect-free layer stack (pH 5) or when the concentration of protons is high enough (pH 2) to stabilize the layer stacking through H-bonds.

By analogy with the origin of the well-defined stacking faults in the 1H HBi phase, one may assume that the presence of Pb and Cd cations in solution significantly decreases proton sorption because of the competition between Me and protons, thus decreasing the reaction rate. As a consequence, most adjacent layers in PbBi and CdBi have the opportunity to be additionally shifted by ±a/3 to build up a defect-free layer stack by

forming strong H-bonds. Both the low amount of interlayer protons and the significant proportion of $Na_{interlayer}$ present in 1H PbBi in comparison with HBi pH 4 support this hypothesis of a slow NaBu-to-MeBi transformation rate.

In contrast to 1H MeBi, ZnBi samples contain a significant amount of orthogonal layer pairs, as the proportion of well-defined stacking faults in samples 1M ZnBi 122 (12%) and 128 (15%) is twice that in CdBi (7%). Moreover, the proportion of such stacking faults dramatically increases with decreasing content of Zn (see XRD pattern of ZnBi 8; Fig. 1b). This peculiar tendency to form defective layer stacking is likely induced by the coexistence of three competitive reactions during the NaBu-to-ZnBi transformation. The first reaction tends to form 1M layer pairs in which adjacent layers are shifted by $+\mathbf{a}/3$ because the presence of ^{IV}Zn in TC sites permits the formation of strong H-bonds between adjacent layers. At high pH, such as those measured when the NaBu-to-ZnBi transformation begins, the common presence of ^{IV}Zn is shown by, for example, the formation of synthetic Zn-Ni hydroxy double salts, $Ni_{1-x}Zn_{2x}(OH)_2(CH_3CO_2)_{2x}.nH_2O$, in which ^{IV}Zn is located just above and below vacant octahedra of the $Ni_{1-x}(OH)_2$ brucite-like layer (Choy et al. 1998). The second reaction also tends to form such 1M layer pairs because only this interlayer configuration allows a chalcophanite-like distribution of vacant layer sites capped on both sides by ^{VI}Zn as discussed by Drits et al. (2002). The third reaction tends to form orthogonal layer pairs because the presence of octahedrally coordinated $Mn^{3+}_{interlayer}$ and Zn leads to the formation of strong H-bonds in such 1H layer pairs (Lanson et al. 2000). This hypothesis is supported by the higher proportion of 1H layer pairs in ZnBi 8 as compared with ZnBi 122 (Fig. 1b) in agreement with their contrasting Zn content.

NaBu-to-MeBi structural transformation

As shown previously, the formation of strong H-bonds between adjacent layers, the minimization of cation electrostatic repulsion, and the nature of sorbed metal cations are key interdependent factors that control the layer stacking mode in the MeBi structure. The low-pH equilibration of NaBu induces a modification of the layer stacking mode to allow the formation of strong H-bonds between adjacent layers (Lanson et al. 2000) because the $-\mathbf{a}/3$ shift between adjacent layers of the NaBu idealized structure (Lanson, unpublished data) is unfavorable for such H-bonds. The energy necessary to transform 1M NaBu into 1H MeBi is minimized if the $n + 1$ and $n + 2$ layers are shifted by $+\mathbf{a}/3$ and $-\mathbf{a}/3$, respectively (Fig. 15 in Lanson et al. 2000). A similar modification of the layer stacking is observed in PbBi and CdBi.

In contrast, the 1M ZnBi structure, in which adjacent layers are shifted with respect to each other by $+\mathbf{a}/3$, may be obtained from the displacement of $n + 1$ and $n + 2$ layers of the initial NaBu crystal by $-\mathbf{a}/3$ and $+\mathbf{a}/3$, respectively. Because these two translations minimize the electrostatic repulsion of layer and interlayer cations equally, the origin of this different layer stacking modification, as compared with that observed for HBi, PbBi, and CdBi, remains unclear, as resulting H-bonds are weak. However, one may note that the interlayer displacement in 1M ZnBi is similar to that in the chalcophanite structure (Wadsley

1955; Post and Appleman 1988). Moreover, interpretation of SAED patterns of ZnBi 69, 122, and 128 samples has shown that the NaBu-to-ZnBi transformation is accompanied, for most particles, by the formation of vacant layer sites distributed as in chalcophanite with an $A = B = b\sqrt{7} = 7.536$ Å, $\gamma = 120°$ unit cell (Drits et al. 2002). These authors have shown that such a distribution of vacant layer sites capped by Zn on both sides is compatible only with the $+\mathbf{a}/3$ displacement between adjacent layers. Therefore, it is likely that the main factor controlling the layer stacking mode in ZnBi is the tendency toward a chalcophanite-like distribution of Zn in interlayers.

REFERENCES CITED

Allman, M. (1969) Verfeinerung der Struktur des Zinc hydroxidchlorids: II. $Zn_5(OH)_8Cl_2H_2O$. Zeitschrift für Kristallographie, 126, 417–427.

Appelo, C.A.J. and Postma, D. (1999) A consistent model for surface complexation on birnessite (δ-MnO_2) and its application to a column experiment. Geochimica et Cosmochimica Acta, 63, 3039–3048.

Balistrieri, L.S. and Murray, J.W. (1982) The surface chemistry of δMnO_2 in major ion seawater. Geochimica et Cosmochimica Acta, 46, 1041–1052.

Bendell-Young, L.I. and Harvey, H.H. (1992) The relative importance of manganese and iron oxides and organic matter in the sorption of trace metals by surficial lake sediments. Geochimica et Cosmochimica Acta, 56, 1175–1186.

Bidoglio, G., Gibson, P.N., O'Gorman, M., and Roberts, K.J. (1993) X-ray absorption spectroscopy investigation of surface redox transformations of thallium and chromium on colloidal mineral oxides. Geochimica et Cosmochimica Acta, 57, 2389–2394.

Brindley, G.W. (1980) Order-disorder in clay mineral structures. In G.W. Brindley and G. Brown, Eds., Crystal Structures of Clay Minerals and their X-ray Identification, p. 125–195. Mineralogical Society, London.

Burns, R.G. and Burns, V.M. (1976) Mineralogy of ferromanganese nodules. In G.P. Glasby, Ed., Marine manganese deposits, p. 185–248. Elsevier, Amsterdam.

——— (1977) The mineralogy and crystal chemistry of deep-sea manganese nodules, a polymetallic resource of the twenty-first century. Philosophical Transactions of the Royal Society of London (A), 286, 283–301.

Burns, V.M. and Burns, R.G. (1978) Post-depositional metal enrichment processes inside manganese nodules from the North Equatorial Pacific Ocean. Earth & Planetary Science Letters, 39, 341–348.

Catts, J.G. and Langmuir, D. (1986) Adsorption of Cu, Pb and Zn by $\delta MnO2$: Applicability of the site binding-surface complexation model. Applied Geochemistry, 1, 255–264.

Chen, R., Chirayil, T., Zavalij, P., and Whittingham, M.S. (1996) The hydrothermal synthesis of sodium manganese oxide and a lithium vanadium oxide. Solid State Ionics, 86–88, 1–7.

Ching, S., Landrigan, J.A., Jorgensen, M.L., Duan, N., Suib, S.L., and O'Young, C.L. (1995) Sol-Gel synthesis of birnessite from $KMnO_4$ and simple sugars. Chemistry of Materials, 7, 1604–1606.

Chorover, J. and Amistadi, M.K. (2001) Reaction of forest floor organic matter at goethite, birnessite and smectite surfaces. Geochimica et Cosmochimica Acta, 65, 95–109.

Choy, J.H., Kwon, Y.M., Han, K.S., Song, S.W., and Chang, S.H. (1998) Intra- and inter-layer structures of layered hydroxy double salts, $Ni_{1-x}Zn_{2x}(OH)_2$ $(CH_3CO_2)_{2x}.nH_2O$. Materials Letters, 34, 356–363.

Chukhrov, F.V. and Gorshkov, A.I. (1981) Iron and manganese oxide minerals in soils. Transactions of the Royal Society of Edinburgh, 72, 195–200.

Chukhrov, F.V., Gorshkov, A.I., Rudnitskaya, E.S., and Sivtsov, A.V. (1978) Birnessite characterization. Investiya Akademie Nauk, SSSR, Seriya Geologicheskaya, 9, 67–76.

Chukhrov, F.V., Sakharov, B.A., Gorshkov, A.I., Drits, V.A., and Dikov, Y.P. (1985) Crystal structure of birnessite from the Pacific ocean. International Geology Review, 27, 1082–1088.

Chukhrov, F.V., Gorshkov, A.I., Berezovskaya, V.V., and Sistov, A.V. (1987) New data about mineralogy of Kertch ore deposits. Izvestiya Akademie Nauk, SSSR, Seriya Geologicheskaya, 4, 60–77.

Chukhrov, F.V., Gorshkov, A.I., and Drits, V.A. (1989) Supergenic manganese hy-

drous oxides. 208 p. Nauka, Moscow.

Cornell, R.M. and Giovanoli, R. (1988) Transformation of hausmannite into birnessite in alkaline media. Clays & Clay Minerals, 36, 249–257.

Daus, B., Mattusch, J., Paschke, A., Wennrich, R., and Weiss, H. (2000) Kinetics of the arsenite oxidation in seepage water from a tin mill tailings pond. Talanta, 51, 1087–1095.

Drits, V.A. and McCarty, D.K. (1996) The nature of diffraction effects from illite and illite-smectite consisting of interstratified trans-vacant and cis-vacant 2:1 layers: A semi-quantitative technique for determination of layer-type content. American Mineralogist, 81, 852–863.

Drits, V.A. and Tchoubar, C. (1990) X-ray diffraction by disordered lamellar structures: Theory and applications to microdivided silicates and carbons. 371 p. Springer-Verlag, Berlin.

Drits, V.A., Petrova, V., and Gorshkov, A.I. (1985) Manganese minerals of Fe-Mn nodules from the sediments of the central part of Pacific Ocean and their post-sedimentation transformation. Lithology and Raw Materials, 3, 17–39.

Drits, V.A., Silvester, E.J., Gorshkov, A.I., and Manceau, A. (1997) The structure of monoclinic Na-rich birnessite and hexagonal birnessite. Part 1. Results from X-ray diffraction and selected area electron diffraction. American Mineralogist, 82, 946–961.

Drits, V.A., Lanson, B., Gorskhov, A.I., and Manceau, A. (1998a) Sub- and super-structure of four-layer Ca-exchanged birnessite. American Mineralogist, 83, 97–118.

Drits, V.A., Eberl, D.D., and Srodon, J. (1998b) XRD measurement of mean thickness, thickness distribution and strain for illite and illite-smectite crystallites by the Bertaut-Warren-Averbach technique. Clays & Clay Minerals, 46, 38–50.

Drits, V.A., Lanson, B., Bougerol-Chaillout, C., Gorshkov, A.I., and Manceau, A. (2002) Structural chemistry of heavy metal sorbed birnessite: Part 2. Results from electron diffraction. American Mineralogist, 87, 1646–1661.

Ghose, S. (1964) The crystal structure of hydrozincite, $Zn_5(OH)_6(CO_3)_2$. Acta Crystallographica, 17, 1051–1057.

Giovanoli, R., Stähli, E., and Feitknecht, W. (1970a) Über Oxidhydroxide des vierwertigen Mangans mit Schichtengitter. 1. Mitteilung: Natrium-mangan(II,III)manganat(IV). Helvetica Chimica Acta, 53, 209–220.

——— (1970b) Über Oxidhydroxide des vierwertigen Mangans mit Schichtengitter. 2. Mitteilung: Mangan(III)-manganat(IV). Helvetica Chimica Acta, 53, 453–464.

Glover, E.D. (1977) Characterization of a marine birnessite. American Mineralogist, 62, 278–285.

Gray, M. and Malati, M.A. (1979) Adsorption from aqueous solution by d-manganese dioxide. II. Adsorption of some heavy metal cations. Journal of Chemical Technology and Biotechnology, 29, 135–144.

Healy, T.W., Herring, A.P., and Fuerstenau, D.W. (1966) The effect of crystal structure on the surface properties of a series of manganese dioxides. Journal of Colloid and Interface Science, 21, 435–444.

Hill, R.J. (1980) The structure of mooreite. Acta Crystallographica, B36, 1304–1311.

Hoffman, C., Armbinster, T., and Giester, G. (1997) Acentric structure (P3) of bechererite, $Zn_7Cu(OH)_{13}[SiO(OH)_3SO_4]$. American Mineralogist, 82, 1014–1018.

Kim, S.H., Kim, S.J., and Oh, S.M. (1999) Preparation of layered MnO_2 via thermal decomposition of $KMnO_4$ and its electrochemical characterizations. Chemistry of Materials, 11, 557–563.

Kuma, K., Usui, A., Paplawsky, W., Gedulin, B., and Arrhenius, G. (1994) Crystal structures of synthetic 7 Å and 10 Å manganates substituted by mono- and divalent cations. Minerogical Magazine, 58, 425–447.

Lanson, B., Drits, V.A., Silvester, E.J., and Manceau, A. (2000) Structure of H-exchanged hexagonal birnessite and its mechanism of formation from Na-rich monoclinic buserite at low pH. American Mineralogist, 85, 826–838.

Lanson, B., Drits, V.A., Feng, Q., and Manceau, A. (2002) Crystal structure determination of synthetic Na-rich birnessite: Evidence for a triclinic one-layer cell. American Mineralogist, 87, 1662–1671.

Le Goff, P., Baffier, N., Bach, S., and Pereira-Ramos, J.-P. (1996) Synthesis, ion exchange and electrochemical properties of lamellar phyllomanganates of the birnessite group. Materials Research Bulletin, 31, 63–75.

Luo, J. and Suib, S.L. (1997) Formation and transformation of mesoporous and layered-manganese oxides in the presence of long-chain ammonium hydroxides. Journal of the Chemical Society, Chemical Communications, 1031–1032.

Mackenzie, R.C. (1970) Simple phyllosilicates based on gibbsite- and brucite-like sheets. In R.C. Mackenzie, Ed., Differential Thermal Analysis: Volume 1, Fundamental Aspects, p. 497–537. Academic Press, New York.

Manceau, A. and Charlet, L. (1992) X-ray absorption spectroscopic study of the sorption of Cr(III) at the oxide-water interface. Journal of Colloid and Interface Science, 148, 425–442.

Manceau, A., Drits, V.A., Silvester, E.J., Bartoli, C., and Lanson, B. (1997) Structural mechanism of Co²⁺ oxidation by the phyllomanganate buserite. American Mineralogist, 82, 1150–1175.

Manceau, A., Lanson, B., Schlegel, M.L., Hargé, J.-C., Musso, M., Eybert-Bérard, L., Hazemann, J.-L., Chateigner, D., and Lamble, G.M. (2000) Chemical forms of trace metals in soils by XAFS spectroscopy. I. Quantitative Zn speciation in smelter-contaminated soils. American Journal of Science, 300, 289–343.

Manceau, A., Lanson, B., and Drits, V.A. (2002) Structure of heavy metal sorbed birnessite: Part 3. Results from powder and polarized EXAFS spectroscopy. Geochimica et Cosmochimica Acta, 66, 2639–2663.

McKenzie, R.M. (1967) The sorption of cobalt by manganese minerals in soils. Australian Journal of Soil Research, 5, 235–246.

——— (1980) The adsorption of lead and other heavy metals on oxides of manganese and iron. Australian Journal of Soil Research, 18, 61–73.

Murray, J.W. (1974) The surface chemistry of hydrous manganese dioxide. Journal of Colloid and Interface Science, 46, 357–371.

Nico, P.S. and Zasoski, R.J. (2000) Importance of Mn(III) availability on the rate of Cr(III) oxidation on δ-MnO_2. Environmental Science and Technology, 34, 3363–3367.

Novikov, G.V. and Cherkashev, G.A. (2000) Ion-exchange reactions on low-temperature oceanic hydrothermal rocks. Geochemistry International, 38 Supplementery issue 2, S194–S205.

Oscarson, D.W., Huang, P.M., Liaw, W.K., and Hammer, U.T. (1983) Kinetics of oxidation of arsenite by various manganese dioxides. Soil Science Society of America Journal, 47, 644–648.

Paterson, E., Swaffield, R., and Clark, L. (1994) The influence of structure on Ba and K uptake by a synthetic phyllomangante. Clay Minerals, 29, 215–222.

Pizzigallo, M.D.R., Ruggiero, P., Crecchio, C., and Mascolo, G. (1998) Oxidation of chloroanilines at metal oxide surfaces. Journal of Agricultural and Food Chemistry, 46, 2049–2054.

Post, J.E. (1999) Manganese oxide minerals: Crystal structures and economic and environmental significance. Proceedings of the National Academy of Sciences of the USA, 96, 3447–3454.

Post, J.E. and Appleman, D.E. (1988) Chalcophanite, $ZnMn_3O_7·3H_2O$: New crystal-structure determinations. American Mineralogist, 73, 1401–1404.

Post, J.E. and Veblen, D.R. (1990) Crystal structure determinations of synthetic sodium, magnesium, and potassium birnessite using TEM and the Rietveld method. American Mineralogist, 75, 477–489.

Rouse, R.C. (1971) The crystal structure of quenselite. Zeitschrift für Kristallographie, 134, 321–332.

Shannon, R.D. (1976) Revised effective ionic radii and systematic studies of interatomic distances in halides and chalcogenides. Acta Crystallographica, A32, 751–767.

Silvester, E.J., Charlet, L., and Manceau, A. (1995) The mechanism of chromium(III) oxidation by Na-buserite. Journal of Physical Chemistry, 99, 16662–16772.

Silvester, E.J., Manceau, A., and Drits, V.A. (1997) The structure of monoclinic Na-rich birnessite and hexagonal birnessite. Part 2. Results from Chemical Studies and EXAFS Spectroscopy. American Mineralogist, 82, 962–978.

Spadini, L., Manceau, A., Schindler, P.W., and Charlet, L. (1994) Structure and stability of Cd²⁺ surface complexes on ferric oxides. Journal of Colloid and Interface Science, 167, 73–86.

Stählin, W. and Oswald, H.R. (1970) The crystal structure of zinc hydroxide nitrate, $Zn_5(OH)_8(NO_3)_2(H_2O)_2$. Acta Crystallographica, B26, 860–863.

Stone, A.T. and Morgan, J.J. (1984) Reductive dissolution of manganese (III) and manganese (IV) oxides by organics. Environmental Science & Technology, 18, 617–624.

Stone, A.T. and Ulrich, H.J. (1989) Kinetics and reaction stoichiometry in the reductive dissolution of manganese(IV) dioxide and cobalt(III) oxide by hydroquinone. Journal of Colloid and Interface Science, 132, 509–522.

Strobel, P., Charenton, J.-C., and Lenglet, M. (1987) Structural chemistry of phyllomanganates: Experimental evidence and structural models. Revue de Chimie Minérale, 24, 199–220.

Stumm, W. (1992) Chemistry of the solid-water interface and particle-water interface in natural systems. 428 p. Wiley, New York.

Taylor, R.M. and McKenzie, R.M. (1966) The association of trace elements with manganese minerals in Australian soils. Australian Journal of Soil Research, 4, 29–39.

Taylor, R.M., McKenzie, R.M., and Norrish, K. (1964) The mineralogy and chemistry of manganese in some Australian soils. Australian Journal of Soil Research, 2, 235–248.

Treiman, A.H. and Peacor, D.R. (1982) The crystal structure of lawsonbauerite, $(Mn, Mg)_9Zn_4(SO_4)_2(OH)22·8H_2O$, and its relation to mooreite. American Mineralogist, 67, 1029–1034.

Tu, S., Racz, G.J., and Goh, T.B. (1994) Transformations of synthetic birnessite as affected by pH and manganese concentration. Clays & Clay Minerals, 42, 321–330.

Wadsley, A.D. (1955) The crystal structure of chalcophanite, $ZnMn_3O_7·3H_2O$. Acta Crystallographica, 8, 165–172.